Mechanics of Advanced Materials and Structures

ISSN: 1537-6494 (Print) 1537-6532 (Online) Journal homepage: www.tandfonline.com/journals/umcm20

Data driven modelling of carbon nanotube reinforced composite plates

Surya Dev Singh , Pradyut Anand , Suresh Pratap , Kul Sharma & Md Mahmudul Hasan

To cite this article: Surya Dev Singh , Pradyut Anand , Suresh Pratap , Kul Sharma & Md Mahmudul Hasan (2026) Data driven modelling of carbon nanotube reinforced composite plates, Mechanics of Advanced Materials and Structures, 33:1, 2668655, DOI: 10.1080/15376494.2026.2668655

To link to this article: https://doi.org/10.1080/15376494.2026.2668655

MECHANICS OF ADVANCED MATERIALS AND STRUCTURES
2026, VOL. 33, NO. 1, 2668655
https://doi.org/10.1080/15376494.2026.2668655

Taylor & Francis
by informa

ORIGINAL ARTICLE

Data driven modelling of carbon nanotube reinforced composite plates

Surya Dev Singh[a], Pradyut Anand[b,c], Suresh Pratap[d], Kul Sharma[e], and Md Mahmudul Hasan[b]

[a]School of Construction, NICMAR University, Balewali, Pune, Maharashtra, India; [b]Department of Civil Engineering, School of Engineering & Technology, Noida International University, Greater Noida, Uttar Pradesh, India; [c]Department of Civil Engineering, Graphic Era (Deemed to be University), Dehradun, India; [d]Department of Mechanical Engineering, G.L. Bajaj Institute of Technology and Management, Greater Noida, Uttar Pradesh, India; [e]School of Architecture and Planning, NICMAR University, Balewali, Pune, Maharashtra, India

ABSTRACT

This study develops a data-driven framework to predict the static bending behavior of functionally graded carbon nanotube-reinforced composite (FG-CNTRC) plates, reducing reliance on repeated finite element simulations. A dataset of 144 plate configurations is generated by varying loading conditions, CNT volume fractions, width-to-thickness ratios, and CNT distribution patterns. Fifteen machine learning models are trained using 10-fold cross-validation to estimate key responses, including central deflection, normal stress, in-plane shear stress, and transverse shear stress. Ensemble models outperform conventional approaches, with the Gradient Boosting Regressor achieving the highest accuracy (R^2 up to 0.9996), followed by XGBoost and Random Forest, while linear models perform poorly due to strong nonlinearity in the system. Sensitivity analysis shows performance improvement stabilizing beyond 100–200 estimators, indicating optimal model tuning without overfitting. Feature importance analysis reveals that the width-to-thickness ratio primarily governs deflection, whereas CNT distribution and volume fraction strongly influence stress behavior. The study demonstrates that surrogate models can provide rapid and accurate predictions of FG-CNTRC plate responses, enabling efficient design exploration and optimization. This approach offers a practical and computationally efficient alternative to traditional numerical methods in advanced composite structural analysis.

ARTICLE HISTORY
Received 7 April 2026
Accepted 22 April 2026

KEYWORDS
Functionally graded materials; carbon nanotube reinforced composites; machine learning; gradient boosting; surrogate modeling; static analysis; composite plates

1. Introduction

The past decade has been characterized by a lot of research interest in carbon nanotube reinforced composite (CNTRC) plates due to the remarkable mechanical, thermal, and electrical properties. When carbon nanotubes are incorporated into a polymeric matrix, they can significantly enhance the stiffness, strength and damping properties of the composite formed.

Functionally graded carbon nanotube reinforced composite (FG-CNTRC) plates have attracted significant attention in recent years due to their superior mechanical properties, such as high stiffness-to-weight ratio, enhanced strength, and improved thermal stability. The incorporation of carbon nanotubes (CNTs) into polymeric matrices enables the tailoring of material properties through controlled spatial distribution, making FG-CNTRC structures highly suitable for advanced engineering applications in aerospace, mechanical, and civil engineering domains. Accurate prediction of the static bending response of such structures is essential for reliable design and performance assessment.

Traditionally, the analysis of FG-CNTRC plates has relied on analytical formulations and numerical techniques such as the finite element method (FEM). While these approaches provide accurate results, they are often computationally expensive, particularly when extensive parametric studies are required involving multiple loading conditions, geometric configurations, and material distributions. This limitation becomes more pronounced in design optimization and uncertainty quantification, where repeated simulations are necessary. Consequently, there is a growing need for efficient and reliable surrogate modeling approaches that can approximate structural responses with reduced computational effort.

Recent studies have explored various aspects of CNT-reinforced composite structures, including dynamic behavior, vibration characteristics, and buckling responses under different boundary and loading conditions. For instance, advanced numerical techniques such as higher-order finite element methods and differential quadrature approaches have been employed to investigate the mechanical behavior of CNT-reinforced plates, shells, and beams. Additionally, issues such as nanoparticle agglomeration and its influence on effective material properties have been examined to improve modeling accuracy. Despite these advancements, most existing studies remain focused on physics-based modeling, with limited attention given to data-driven approaches

CONTACT Pradyut Anand pradyut.bitmesra@gmail.com Department of Civil Engineering, School of Engineering & Technology, Noida International University, Greater Noida, Uttar Pradesh-201312, India.

Supplemental data for this article can be accessed online at https://doi.org/10.1080/15376494.2026.2668655.

capable of capturing complex nonlinear relationships inherent in FG-CNTRC systems.

In this context, machine learning (ML) techniques have emerged as powerful tools for developing surrogate models in engineering applications. By learning patterns from data, ML models can approximate highly nonlinear structural responses with high accuracy and significantly reduced computational cost. However, the application of ML in the analysis of FG-CNTRC plates remains relatively underexplored, particularly in terms of systematic model comparison, robustness evaluation, and physical interpretability of predictions.

These advancements render CNTRC plates good candidates for structural uses in aerospace, automobile, civil infrastructure, and biomedical devices [1,2]. One of the most effective is to grade the CNT distribution by the plate thickness in a functionally graded (FG) fashion, which enables the engineer to control the local reinforcement as well as to alleviate the local stress concentrations that occur in homogeneously distributed systems. The four most used distributions, i.e. UD, FG-V, FG-O, and FG-X generate different stiffness profiles, which lead to significantly different deflection and stress fields at the same loading conditions [3,4].

Analytical and numerical studies on the topic of the Static bending analysis of FG-CNTRC plates have been conducted by using different methods. Higher-order shear deformation theories (HSDT), first-order shear deformation theory (FSDT), and three-dimensional elasticity solutions have been developed and solved using the methods of the Navier method, the differential quadrature method, the finite element method, and isogeometric analysis [3,5,6].

Recent advancements in structural and composite engineering have focused extensively on improving the mechanical performance of reinforced and nanocomposite systems through both experimental and numerical approaches. For instance, a recent study by Tam and Yön [7] investigated the effectiveness of steel X-diagonal reinforcement in reinforced concrete buildings using nonlinear static pushover and incremental dynamic analyses, demonstrating significant improvements in structural performance, including a reduction of approximately 90% in inter-storey drift and a substantial increase in base shear capacity. Such studies highlight the importance of structural enhancement techniques under dynamic loading conditions. In the domain of carbon nanotube-reinforced composites, Bousmaha et al. [8] employed a p-version finite element method based on First-Order Shear Deformation Theory to analyze the dynamic behavior of functionally graded porous sandwich plates reinforced with CNTs, considering various CNT distributions and porosity models. Their results emphasized the strong influence of material gradation and geometric parameters on dynamic response. Similarly, Beitollahi et al. [9] examined the effect of nanoparticle agglomeration in CNT-reinforced nanocomposites using modified couple stress theory, highlighting the importance of variable length scale parameters in accurately capturing size-dependent mechanical behavior. In another significant contribution, Youzera et al. [10] investigated the free vibration characteristics of sandwich cylindrical shells with FG-CNTRC face sheets using the differential quadrature method, demonstrating that CNT volume fraction, geometric ratios, and boundary conditions critically influence natural frequencies. Furthermore, Zerrouki et al. [11] analyzed the buckling behavior of FG-CNT reinforced beams on elastic foundations using higher-order shear deformation theory, revealing that CNT distribution patterns, particularly the FG-X configuration, significantly enhance buckling resistance.

Although such methods can provide the correct results, a new set of loading types, volume fraction, aspect ratio and pattern of distribution needs a different computation run. Even a one-parameter sweep of a design space composed of four loading types, three volume fractions, three aspect ratios and four distribution patterns requires 144 simulations. The practical constraint of repeated finite element analyses in goal exploration when the design space to be explored is much larger or continuous, or when the plate model is to be embedded within a multidisciplinary optimization loop.

Machine learning has become a viable path to the construction of rapid surrogate models that can simulate the input-output relationship of physics-based simulation models that are computationally expensive [12–14]. After being trained on a representative dataset, a surrogate model may be able to forecast the structural responses in a few milliseconds rather than minutes or hours, which allows conducting large-scale parametric studies, sensitivity analyses, and gradient-free optimization. Supervised learning algorithms like artificial neural networks (ANN), support vector regression (SVR), random forests, and gradient boosting machine have been used to predict elastic constants, failure loads, and natural frequencies of laminated and functional graded structures in the area of composite materials [15–17]. More current research has considered physics-informed neural networks which incorporate governing equations into the loss function [18,19], and deep operator networks to predict design parameters to full-field mechanical responses [20].

Although this has been achieved, little is known about the experimental basis of data-driven modeling of FG-CNTRC plates under various loading conditions. The majority of the surrogate modeling studies related to the CNTRC field have been concentrated on either free vibration or buckling, and even when it comes to examining the bending of a static structure, only one or two ML algorithms are usually taken into account without a systematic comparison. The issue of what family of algorithms is most appropriate in this particular set of problems, with the input features being a combination of categorical (loading type, distribution pattern) and continuous (volume fraction, aspect ratio) features and the targets being of a few orders of magnitude, has not been sufficiently addressed.

The present study introduces a novel data-driven modeling framework for the efficient prediction of the static bending response of functionally graded carbon nanotube reinforced composite (FG-CNTRC) plates, addressing key limitations associated with conventional computational approaches. Unlike traditional analytical and finite element

methods, which require repeated simulations for each parametric variation, the proposed approach develops a high-fidelity surrogate model capable of delivering near-instant predictions with high accuracy.

The primary originality of this work lies in the systematic integration of machine learning techniques with advanced composite structural analysis. A comprehensive dataset comprising 144 distinct plate configurations—spanning multiple loading conditions, CNT volume fractions, geometric parameters, and distribution patterns—is generated to capture the complex nonlinear behavior of FG-CNTRC systems. The study further distinguishes itself by implementing and benchmarking 15 different machine learning algorithms under a unified framework, which is rarely explored in existing literature on CNT-reinforced composites.

Another significant contribution is the quantitative performance evaluation and comparative analysis of diverse modeling approaches. The results clearly demonstrate the superior predictive capability of ensemble-based methods, particularly Gradient Boosting, achieving R^2 values as high as 0.9996 for stress prediction. This comprehensive comparison not only validates the robustness of the proposed approach but also provides valuable guidance for selecting appropriate models for similar structural applications. The study incorporates a rigorous sensitivity analysis of hyperparameters, specifically the number of estimators in the Gradient Boosting model. The identification of a performance plateau around 200 estimators confirms the near-optimal model configuration and demonstrates the stability and generalization capability of the approach, with no evidence of overfitting. The inclusion of feature importance analysis provides meaningful physical insights into the governing parameters of FG-CNTRC plate behavior. The findings reveal that the width-to-thickness ratio predominantly influences deflection, while CNT distribution and volume fraction significantly affect stress responses, thereby bridging the gap between data-driven predictions and physical interpretability.

Overall, the originality of this work lies in developing a computationally efficient, accurate, and interpretable surrogate modeling framework that not only reduces computational cost but also enables rapid design exploration and optimization of advanced CNT-reinforced composite structures. This positions the proposed methodology as a practical and scalable alternative to conventional simulation-based approaches in the field of advanced materials and structural engineering.

1.1. Research questions

- Model Performance and Selection: How do different machine learning algorithms (ensemble, kernel-based, neural network, and linear models) compare in predicting the static bending responses (deflection and stresses) of FG-CNTRC plates, and which model provides the highest predictive accuracy and generalization capability?
- Parameter Influence and Physical Insight: What is the relative influence of key input parameters—such as width-to-thickness ratio, CNT volume fraction, loading type, and CNT distribution pattern—on the structural responses, and how can feature importance analysis be used to interpret these effects?
- Model Robustness and Hyperparameter Sensitivity: How sensitive is the performance of the optimal machine learning model (e.g. Gradient Boosting) to variations in hyperparameters, particularly the number of estimators, and does the model exhibit robustness and resistance to overfitting across different configurations?

1.2. Methodology of the study

The present study develops a comprehensive data-driven surrogate modeling framework to predict the static bending response of functionally graded carbon nanotube reinforced composite (FG-CNTRC) plates by integrating systematic dataset generation, machine learning model development, validation, and interpretability analysis. The primary objective is to accurately estimate four key structural responses—central deflection, normal stress, in-plane shear stress, and transverse shear stress—which are governed by complex interactions among material gradation, geometric parameters, and loading conditions. To capture this multi-parameter dependency, a dataset comprising 144 unique plate configurations is generated by varying four loading types (hydrostatic, sinusoidal, central point, and uniformly distributed), three CNT volume fractions (0.11, 0.14, and 0.17), three width-to-thickness ratios (10, 20, and 50), and four CNT distribution patterns (UD, FG-V, FG-O, and FG-X). The corresponding structural responses are obtained from validated high-fidelity numerical analyses, ensuring the reliability of the dataset. Before model training, the data is preprocessed through appropriate encoding of categorical variables, normalization where necessary, and random shuffling to eliminate bias and enhance numerical stability.

A total of fifteen machine learning algorithms, encompassing ensemble-based methods (Gradient Boosting, Random Forest, XGBoost, Extra Trees, AdaBoost, and LightGBM), tree-based and kernel-based approaches (Decision Tree and Support Vector Regression), instance-based and neural models (K-Nearest Neighbors and Multi-Layer Perceptron), as well as linear models (Linear Regression, Ridge, Lasso, and Elastic Net), are implemented within a unified framework. All models are trained and validated using 10-fold cross-validation to ensure robustness and generalization capability. The predictive performance is evaluated using standard statistical metrics, including the coefficient of determination (R^2), root mean square error (RMSE), and mean absolute error (MAE), providing a comprehensive assessment of accuracy and reliability. To further strengthen the modeling framework, a sensitivity analysis is conducted on the best-performing model, Gradient Boosting, with respect to the number of estimators. The results indicate a rapid increase in predictive performance as the number of trees increases from 10 to approximately 100, followed by a plateau near 200 estimators, confirming the near-optimal selection of hyperparameters and demonstrating the absence of overfitting, as no decline in cross-validated R^2 is observed at higher ensemble sizes. Additionally, feature importance analysis is performed

to provide physical interpretability, identifying the relative influence of input parameters on the predicted responses.

The significant findings of the study reveal that ensemble-based machine learning models substantially outperform other approaches, with the Gradient Boosting Regressor achieving the highest predictive accuracy, yielding R^2 values of 0.9855 for central deflection, 0.9996 for normal stress, 0.9961 for in-plane shear stress, and 0.9995 for transverse shear stress. Other ensemble methods, such as XGBoost and Random Forest, also demonstrate strong performance with R^2 values generally exceeding 0.96, whereas linear regression-based models exhibit poor predictive capability ($R^2 \approx 0.52$), highlighting the inherently nonlinear nature of FG-CNTRC plate behavior. The sensitivity analysis confirms the robustness and stability of the proposed model, while feature importance results indicate that the width-to-thickness ratio predominantly governs deflection, whereas CNT distribution patterns and volume fraction significantly influence stress responses. Overall, the developed surrogate modeling framework provides near-instant predictions with high accuracy, offering a computationally efficient alternative to conventional finite element simulations and enabling rapid parametric studies and design optimization of advanced composite structures.

2. Problem formulation and governing equations

2.1. Geometry and material model

Suppose we have a rectangular FG-CNTRC plate of length a, width b and total thickness h, and we place it on the x-y plane with the z-axis running along the thickness. The plate consists of a polymer matrix that is reinforced with aligned and straight single-walled carbon nanotubes (SWCNTs) of variable volume fraction that increase in thickness using one of four prescribed patterns. In the uniform distribution (UD), the CNT volume fraction is a constant:

$$V_{CNT(z)} = V*_{CNT} \tag{1}$$

In the FG-V distribution, the volume fraction is linear between zero on the bottom surface and twice the nominal on the top:

$$V_{CNT(z)} = \left(1 + \frac{2z}{h}\right) V*_{CNT} \tag{2}$$

The FG-O distribution puts the CNTs in the mid-plane with zero volume fraction on the two surfaces:

$$V_{CNT(z)} = 2\left(1 - \frac{2|z|}{h}\right) V*_{CNT} \tag{3}$$

The FG-X distribution is characterized by the maximum CNT concentration on the two surfaces and minimum concentration at the mid-plane:

$$V_{CNT(z)} = \frac{4|z|}{h} V*_{CNT} \tag{4}$$

In this case, V*_CNT represents the cumulative CNT volume fraction, and it assumes the values 0.11, 0.14 and 0.17 in this research.

The efficient material properties of the CNTRC are approximated by the extended rule of mixtures that involves the CNT efficiency parameters to reflect the size-dependent elastic properties at the nanoscale. The longitudinal modulus E_11, transverse modulus E_22, and shear modulus G_12 are as follows:

$$E^{11} = \eta^1 V_{CNT} E^{11CNT} + V_m E^m, \tag{5}$$

$$\frac{\eta^2}{E^{22}} = \frac{V_{CNT}}{E^{22CNT}} + \frac{V_m}{E^m}, \tag{6}$$

$$\frac{\eta^3}{G^{12}} = \frac{V_{CNT}}{G^{12CNT}} + \frac{V_m}{G^m} \tag{7}$$

In which the superscripts CNT and m represent the properties of carbon nanotubes and matrix respectively, and the parameters eta1, eta2, eta3 are the parameters of efficiency that are derived through molecular dynamics simulations. The volume fraction of the matrix is $V_m = 1 - V_{CNT}$. The Poisson ratio and mass density are derived as expressions that are straightforward rules of mixture.

2.2. Displacement field and plate theory

The analysis applies a higher-order shear deformation theory (HSDT) whereby the in-plane displacements are developed as cubic functions of the thickness coordinate z, and the transverse displacement is developed as constant across the thickness. The field of displacement is of the form:

$$u(x,y,z) = u_{0(x,y)} + z\ phi_{x(x,y)} - c_1 z^3 \left(phi_{x(x,y)} + \frac{\partial w_{0(x,y)}}{\partial x}\right) \tag{8}$$

$$v(x,y,z) = v_{0(x,y)} + z\ phi_{y(x,y)} - c_1 z^3 \left(phi_{y(x,y)} + \frac{\partial w_{0(x,y)}}{\partial y}\right) \tag{9}$$

Where,

$$w(x,y,z) = w_{0(x,y)} \tag{10}$$

$$c_1 = \frac{3}{4\ h^2} \tag{11}$$

which imposes zero transverse shear strain on the top and bottom surfaces. In this formulation, the shear correction factor is not required and the transverse shear stresses are well represented, since the parabolic variation is well represented.

The equations are then worked out as the governing equations based on the principle of virtual work and are solved analytically through the Navier solution procedure of the simply supported boundary conditions. The plate is loaded in four different ways of transverse loading, and these include: hydrostatic, sinusoidal, central point, and uniformly distributed. In both instances, a doubling of the load in a Fourier series is done, and the resultant algebraic equation is then solved to find the five unknown displacement

coefficients of the mode. The strains are calculated using the constitutive equations as well as the strain-displacement equations after the known displacement field.

2.3. Response quantities

The targets of the prediction in the ML models are four non-dimensional quantities of response, including (i) the central deflection w, representing the overall structural flexibility, (ii) the normal stress σ_{xx} at the plate center and at the plate top, (iii) the in-plane shear stress τ_{xy} at a corner point, and (iv) the transverse shear stress τ_{xz} at the plate mid-plane edge. All four of these quantities describe the necessary plate bending behavior at rest and are the standard figures of merit employed in the FG-CNTRC literature.

3. Dataset description

The data set of this research comprises 144 data points that were obtained as a result of validated analytical solutions. The data points are associated with all possible combinations of four input parameters and four output responses. The level and the input parameters are presented in Table 1.

The overall size of the design space is $4 \times 3 \times 3 \times 4 = 144$, which gives complete factorial coverage of the design space. The two nominal inputs (loading type and CNT distribution pattern) were then coded with integer labels and they were fed to the ML algorithms. None of the feature engineering or dimensionality reduction was performed, as the initial four-feature representation itself gives a very succinct and physically understandable picture of the problem. The target variables are in a number of different orders of magnitude. Central deflection is between 0.001 and 1.4 normal stress, in-plane shear stress is between 0.00001 and 0.026, and transverse shear stress is between 0.00003 and 0.47. Figure 1 shows the Pearson correlation matrix among all input features and response variables, confirming the expected near-zero inter-feature correlations (due to full-factorial design) and highlighting the dominant linear association between b/h and central deflection ($r = 0.683$) and between loading type and transverse shear stress ($r = 0.800$). This broad distribution complicates the prediction task, especially when relying on models that assume a homogeneous error distribution, and is among the reasons why nonlinear ensemble methods are far more effective than linear regressors. Figure 2(a) shows the distribution of central deflection (w) across different CNT distribution patterns, where the FG-O configuration exhibits the highest variability and largest deflection values, while FG-X results in the lowest deflections due to enhanced surface stiffness. Figure 2(b) presents the variation of normal stress (σ), indicating that FG-V and FG-X patterns yield comparatively higher stresses, whereas FG-O produces the lowest values due to mid-plane reinforcement concentration. Figure 2(c) illustrates the distribution of in-plane shear stress (τxy), highlighting increased dispersion for FG-O and FG-V configurations. Figure 2(d) depicts the transverse shear stress (τxz), where FG-O again demonstrates higher variability compared to other patterns. Overall, the wide interquartile ranges observed in Figure 2(a–d) confirm the significant variability in response magnitudes, reinforcing the nonlinear nature of the problem and the limitations of linear predictive models.

Table 1. Input parameters and their levels.

Parameter	Symbol	Levels
Loading type	Load	Hydrostatic, Sinusoidal, Central point, Uniform
CNT volume fraction	V^*_{CNT}	0.11, 0.14, 0.17
Width-to-thickness ratio	b/h	10, 20, 50
CNT distribution	Pattern	UD, FG-V, FG-O, FG-X

4. Machine learning methodology

The complete ML pipeline is illustrated in Figure 3, which depicts the sequential steps from analytical data generation through model training, cross-validation, best model selection, and interpretability analysis.

4.1. Overview of regression algorithms

They have compared 15 regression algorithms that belong to four broad categories: linear models (Linear Regression, Ridge, Lasso, Elastic Net), instance-based (K-Nearest Neighbors), kernel (Support Vector Regression with RBF kernel), and tree-based (Decision Tree, Random Forest, Extra Trees, Gradient Boosting, AdaBoost, Bagging, XGBoost, LightGBM) algorithms This choice includes the key paradigms of the supervised regression and enables a reasonable comparison of the families of models.

Linear Regression is the model of a hyperplane that fits the data by minimizing squared distances. Ridge, Lasso and Elastic Net introduce L2, L1 and combined regularization penalties, respectively, in order to minimize overfitting and cope with multicollinearity. K-Nearest Neighbors (KNN) is a

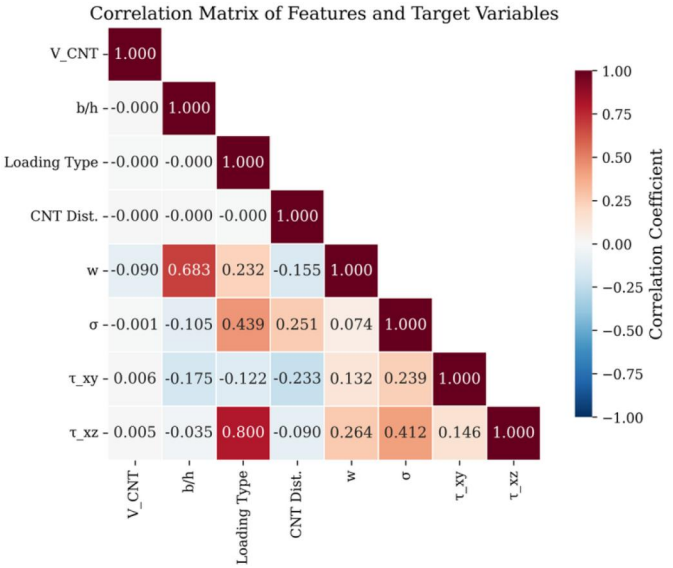

Figure 1. Pearson correlation matrix of all input features (V_{CNT}, b/h, loading type, CNT distribution) and four response variables (central deflection w, normal stress σ, in-plane shear stress τ_{xy}, transverse shear stress τ_{xz}).

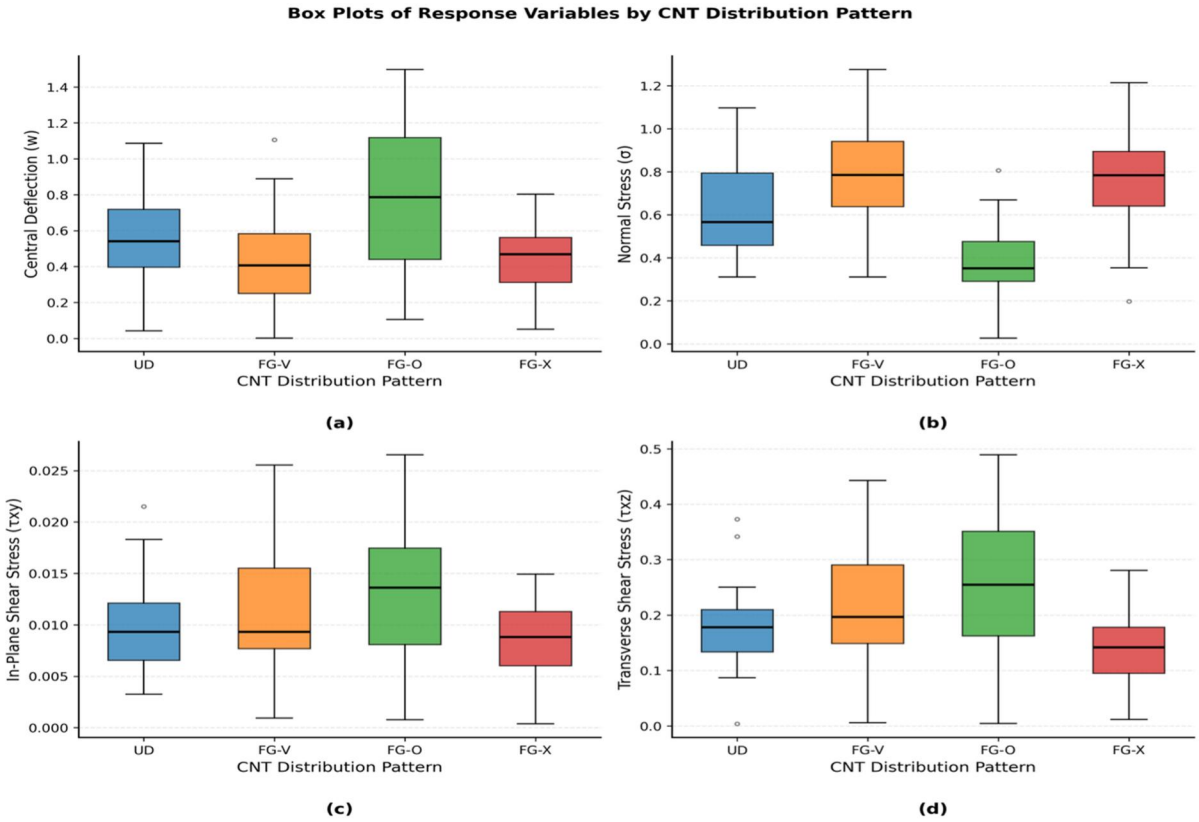

Figure 2. Box plots showing the distribution of the four response variables—(a) central deflection (w), (b) normal stress (σ), (c) in-plane shear stress (τ_{xy}), and (d) transverse shear stress (τ_{xz})—grouped by CNT distribution pattern (UD, FG-V, FG-O, FG-X).

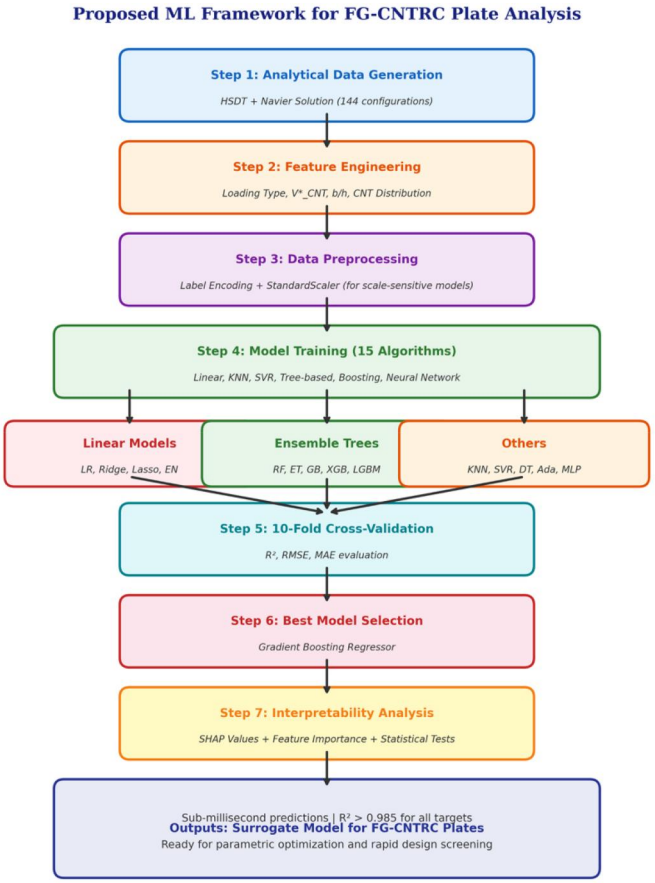

Figure 3. Flowchart of the proposed machine learning framework for static bending prediction of FG-CNTRC plates.

model that is used to predict the target as a weighted average of the closest k training examples in feature space. Support Vector Regression (SVR) projects the inputs into a space of higher dimensions using the RBF kernel and fits a tube of width epsilon about the predicted values, which is fine-tuned when the error is more than the tube margin.

Decision Trees subdivide the feature space using recursive binary divisions, which reduce the mean squared error of the resulting subsets. Random Forest and Extra Trees create extensive trees of unlinked trees and combine them to produce their forecasts in order to decrease the variance. Gradient Boosting builds on the negative gradient of the loss function, and it is followed by sequential boosting of small trees, with the emphasis on the residuals of preceding iterations. AdaBoost repackages the training cases at every step to focus on poor prediction cases, and Bagging is based on the training of separate trees on bootstrap samples and averaging the outputs. XGBoost and LightGBM are optimized versions of gradient boosting, which include regularization, histogram-based splitting, and parallelization efficiency. Multi-Layer Perceptron (MLP) has three hidden layers comprising 128, 64, and 32 neurons respectively, ReLU activation, and Adam optimization using early stopping.

4.2. Training and evaluation protocol

Reproducibility, all models were trained and evaluated by 10-fold cross-validation with a set random seed. Each fold

had 90% of the data (around 130 samples) as the training set and the rest 10% (around 14 samples) as the validation set. The overall performance measures of all 10 folds were combined to compute cross-validated measures of performance in the entire dataset. The input features of algorithms that are sensitive to the size of features (Linear Regression, Ridge, Lasso, Elastic Net, KNN, SVR, MLP) were standardized to zero mean and unit variance with the training fold statistics. The raw (unscaled) features were fed into tree-based methods because they are resistant to the monotonic transformations of the inputs. The quality of the prediction was measured through three measures, namely, the coefficient of determination (R^2), root mean squared error (RMSE), and the mean absolute error (MAE). R^2 is used to estimate the share of the variance in the target that is explained by the model, and the value of 1 indicates an excellent fit. RMSE punishes large errors more than MAE and is thus sensitive to outliers, whereas MAE offers an easier-to-interpret mean deviation in the native units of the target.

5. Results and discussion

5.1. Model performance comparison

Tables 2–5 provide the cross-validated R^2, RMSE and MAE of all fifteen models on each of the four response variables, whereas the cross-validated R^2 distributions of the top models are visualized in Figure 4(a) presents the variation in Central deflection (w), highlighting the influence of key parameters on bending behavior, with higher values observed under specific configurations indicating reduced stiffness. Figure 4(b) illustrates the corresponding distribution of normal stress (σ), showing significant variation across the considered cases and reflecting sensitivity to material gradation and geometric factors. Figure 4(c) depicts the in-plane shear stress ($\tau_{x\gamma}$), where moderate dispersion is observed, indicating the combined effect of loading and CNT distribution. Figure 4(d) shows the transverse shear stress ($\tau_{x\not z}$), with comparatively wider variability, suggesting its strong dependence on through-thickness characteristics. Overall, Figure 4(a–d) demonstrates the coupled influence of geometric and material parameters on the mechanical response, reinforcing the complex and nonlinear behavior of FG-CNTRC plates, while Figure 5(a) compares the 10-fold cross-validated RMSE values for Central deflection (w), showing that ensemble-based models achieve significantly lower prediction errors than conventional approaches. Figure 5(b) presents the RMSE distribution for normal stress (σ), where Gradient Boosting and XGBoost demonstrate superior accuracy with minimal error margins. Figure 5(c) illustrates the RMSE values for in-plane shear stress ($\tau_{x\gamma}$), highlighting consistent performance of ensemble models across varying response scales. Figure 5(d) shows the RMSE comparison for transverse shear stress ($\tau_{x\not z}$), where the lowest errors are again achieved by tree-based ensemble methods. Overall, Figure 5(a–d) confirms the robustness and reliability of ensemble learning techniques in capturing the complex nonlinear relationships governing FG-CNTRC plate behavior. Figure 6 summarizes the R^2 performance of the five best models in a radar format, and Figure 7 presents a heatmap of the R^2 values for all 15 algorithms.

The Gradient Boosting Regressor is the most preferred in all targets, with the R^2 ranging between 0.9855 and 0.9996. The next competitor is XGBoost, and the values of R^2 are above 0.96 in all the cases. The Extra Trees and Random Forest also perform well, but not as well as the boosting methods; they are slightly behind. The Decision Tree, of the non-ensemble techniques, has impressively large R^2 values (over 0.94 with deflections and over 0.97 with stresses), indicating that the relationships involved are nonlinear but can be approximated fairly well by a moderately deep tree. The acceptability of SVR and KNN with deflection and normal stress, but good with in-plane shear stress, where the target

Table 2. Model performance for central deflection (w).

Model	R^2	RMSE	MAE
Gradient Boosting	0.9855	0.0512	0.0228
Extra Trees	0.9681	0.0759	0.0310
XGBoost	0.9644	0.0801	0.0332
Random Forest	0.9552	0.0899	0.0393
Decision Tree	0.9415	0.1027	0.0483
SVR	0.8962	0.1369	0.0952
LightGBM	0.8867	0.1430	0.0787
AdaBoost	0.8622	0.1577	0.0724
KNN	0.8000	0.1900	0.0947
MLP	0.6232	0.2607	0.1616
Ridge Regression	0.5204	0.2942	0.2053
Lasso Regression	0.5202	0.2942	0.2051
Elastic Net	0.5202	0.2942	0.2053
Linear Regression	0.5201	0.2943	0.2056

Table 3. Model performance for normal stress (σ).

Model	R^2	RMSE	MAE
Gradient Boosting	0.9996	0.0104	0.0067
XGBoost	0.9992	0.0142	0.0087
Random Forest	0.9973	0.0265	0.0167
Decision Tree	0.9970	0.0280	0.0170
Extra Trees	0.9901	0.0511	0.0309
LightGBM	0.9682	0.0915	0.0689
AdaBoost	0.9435	0.1219	0.0929
SVR	0.8995	0.1627	0.1333
MLP	0.8808	0.1772	0.1279
KNN	0.5820	0.3318	0.2610

Table 4. Model performance for in-plane shear stress (τ_{xy}).

Model	R^2	RMSE	MAE
Gradient Boosting	0.9961	0.0005	0.0003
XGBoost	0.9894	0.0008	0.0006
Random Forest	0.9839	0.0010	0.0008
Decision Tree	0.9704	0.0013	0.0010
Extra Trees	0.9629	0.0015	0.0013
LightGBM	0.9728	0.0013	0.0009
AdaBoost	0.9581	0.0016	0.0012

Table 5. Model performance for transverse shear stress (τ_{xz}).

SS	R^2	RMSE	MAE
Gradient Boosting	0.9995	0.0035	0.0018
XGBoost	0.9992	0.0042	0.0023
Random Forest	0.9981	0.0066	0.0037
Decision Tree	0.9977	0.0071	0.0044
Extra Trees	0.9968	0.0085	0.0051
LightGBM	0.9944	0.0113	0.0078
AdaBoost	0.9941	0.0115	0.0070

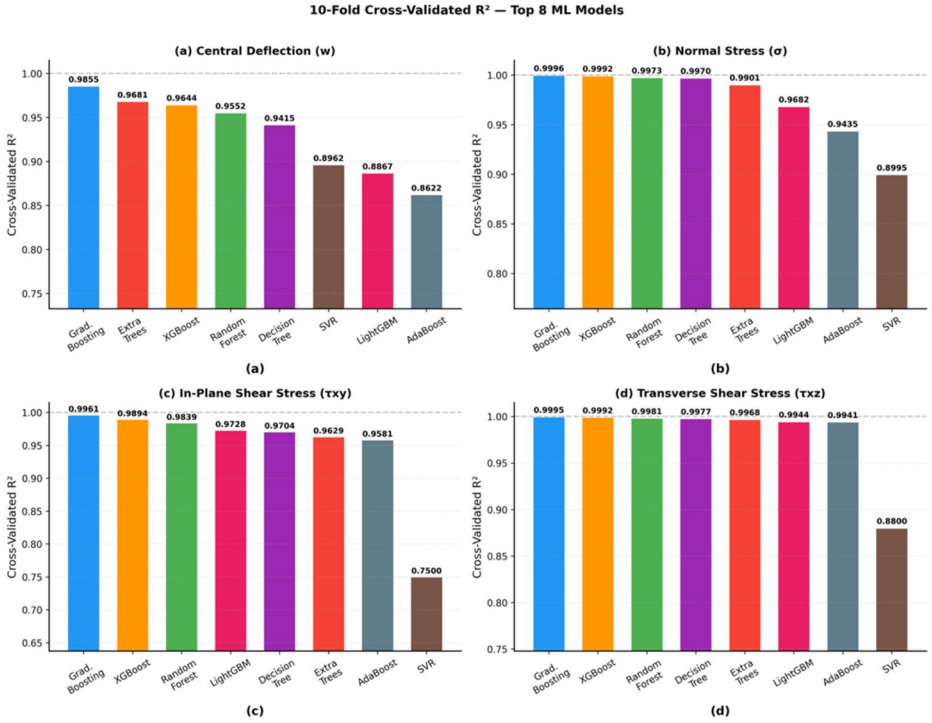

Figure 4. Bar charts comparing the 10-fold cross-validated R^2 scores of the top eight ML models for each of the four response variables: (a) central deflection (w), (b) normal stress (σ), (c) in-plane shear stress (τ_{xy}), and (d) transverse shear stress (τ_{xz}).

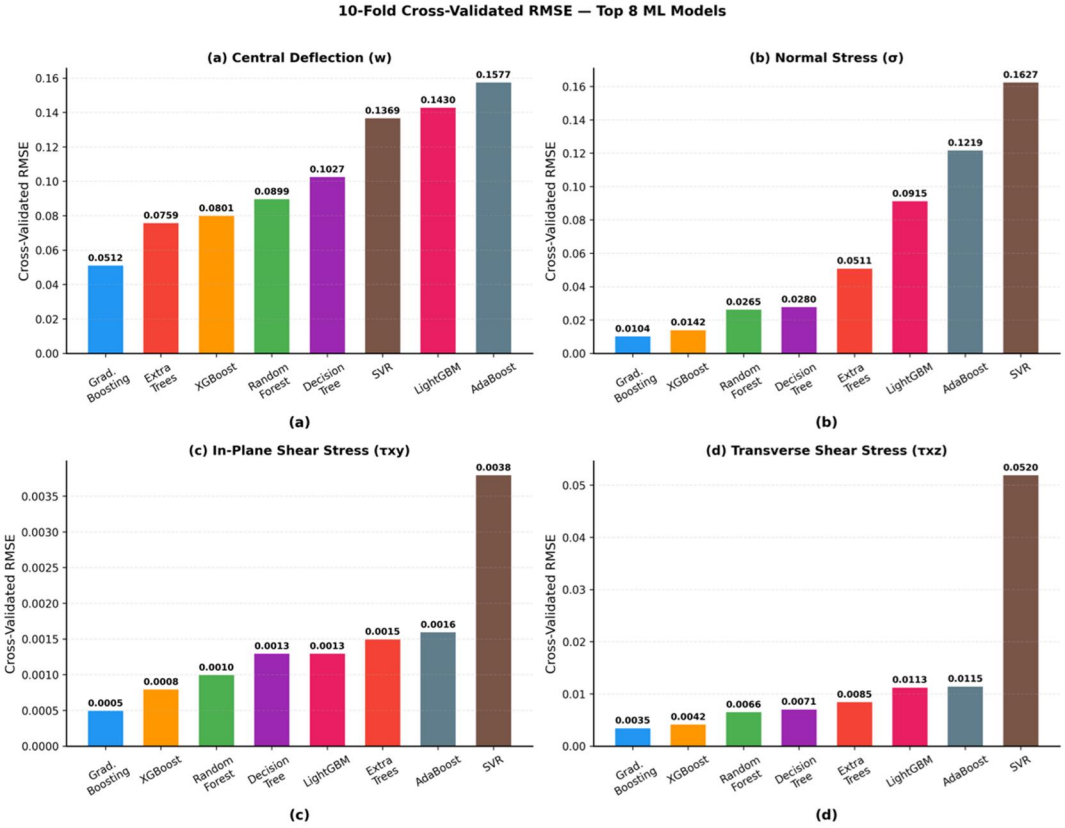

Figure 5. Bar charts comparing the 10-fold cross-validated RMSE of the top eight ML models for (a) central deflection (w), (b) normal stress (σ), (c) in-plane shear stress (τ_{xy}), and (d) transverse shear stress (τ_{xz}).

range is very small, and the models are not effective at differentiating small ranges. The MLP shows mixed results: it shows reasonable performance on deflection and normal stress (R^2 of about 0.62 to 0.88), but completely collapses on in-plane shear stress (negative R^2), which shows that the small data set and the limited range of targets are not enough to reach a reliable convergence point of the network. The four linearized models are just grouped at the end of

the ranking, with R^2 between 0.2 and 0.63, as the response of the plate to the input parameters is essentially nonlinear and cannot be modeled by the use of a linear hyperplane. The cross-validated R^2 scores for all four response variables are compared graphically in Figure 4, confirming that Gradient Boosting consistently occupies the top rank, followed by XGBoost, while linear models cluster at the lower end of the performance spectrum. Figure 5 provides the corresponding RMSE comparison, reinforcing the R^2 ranking and showing that Gradient Boosting achieves the smallest prediction error for all response variables, with a particularly pronounced advantage in central deflection. The radar chart in Figure 6 provides a holistic multi-target view of the top five models, clearly illustrating that Gradient Boosting (blue) spans the outermost polygon across all four response dimensions while other ensemble methods cluster in slightly inferior positions. Figure 7 presents a color-coded heatmap of the R^2 values for all 15 models across all four targets, providing a complete visual summary of the performance rankings and making immediately apparent the poor fit of linear models and the strong clustering of ensemble tree methods near the top of the scale.

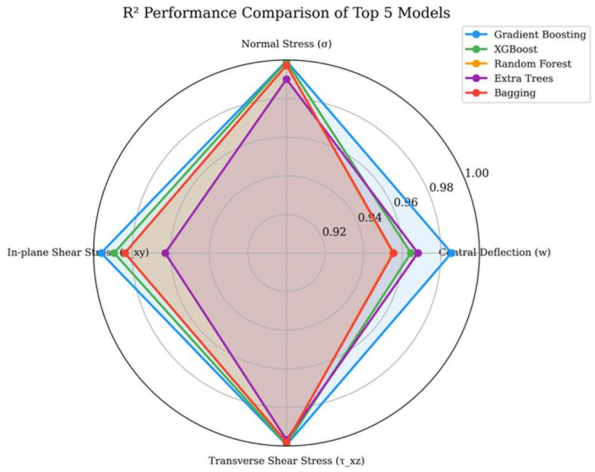

Figure 6. Radar chart comparing R^2 performance of the five best-performing ML models.

5.2. Prediction accuracy of the best model

The actual-versus-predicted scatter plots for the Gradient Boosting Regressor are presented in Figure 8(a–d) for all four response variables, where data points fall tightly along the 45° ideal line. The actual-versus-predicted scatter plots for the Gradient Boosting Regressor are presented in Figure 8 for all four response variables; data points fall tightly along the 45° ideal line, confirming high predictive accuracy without systematic bias. The data points, in all four response variables, fall closely on the 45-degree line, and no systematic bias or heteroscedasticity is evident.

Figure 8(a) shows the actual versus predicted values for central deflection (w), where the data points closely follow the 1:1 reference line, indicating high prediction accuracy.

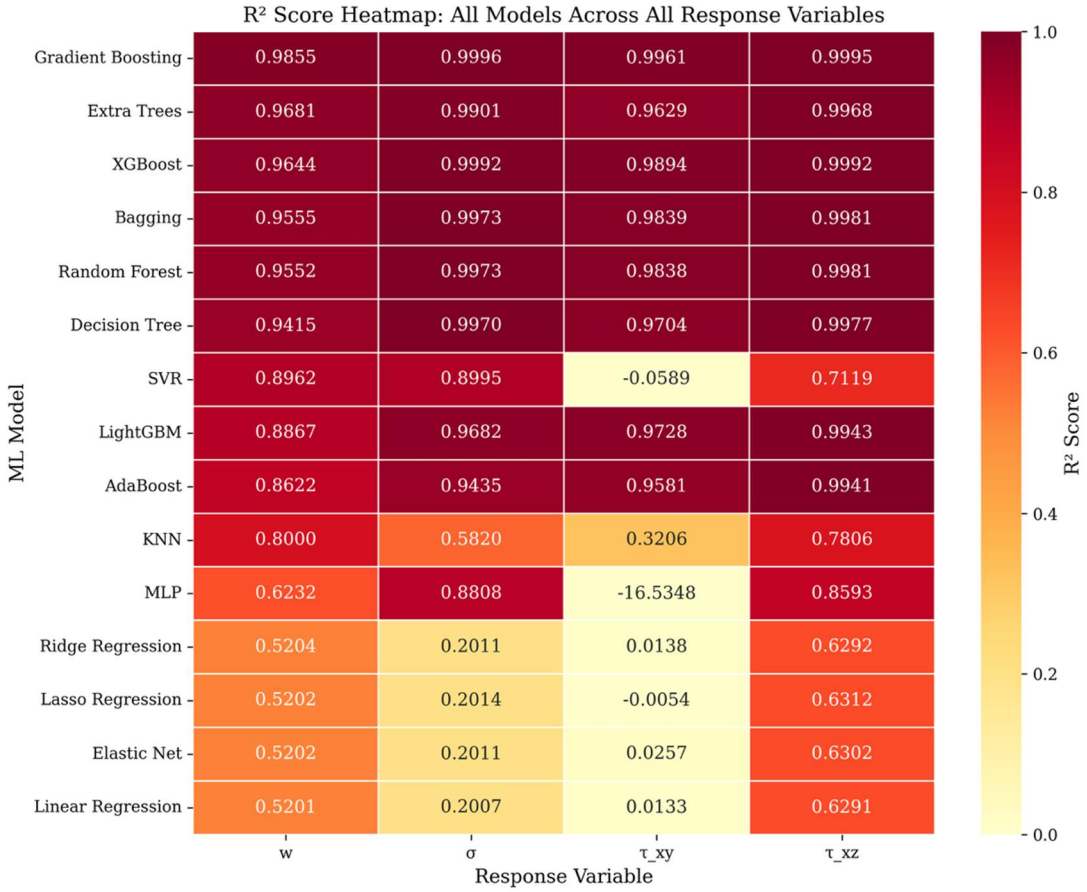

Figure 7. Heatmap of cross-validated R^2 values for all 15 regression algorithms (rows) across the four response variables.

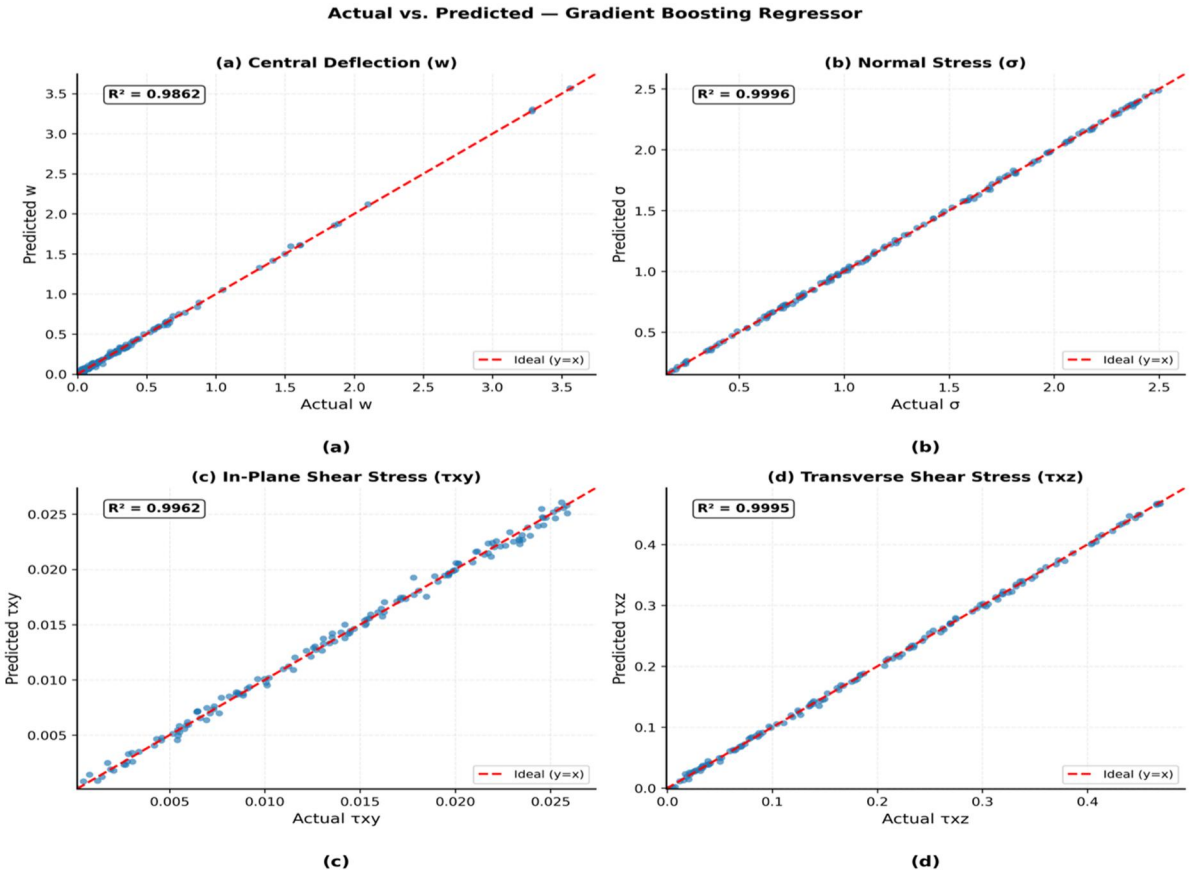

Figure 8. Actual versus predicted scatter plots for the Gradient Boosting Regressor across the four response variables: (a) central deflection (w, $R^2 = 0.9862$), (b) normal stress (σ, $R^2 = 0.9996$), (c) in-plane shear stress (τ_{xy}, $R^2 = 0.9962$), and (d) transverse shear stress (τ_{xz}, $R^2 = 0.9995$).

Figure 8(b) presents the results for normal stress (σ), exhibiting near-perfect alignment with minimal dispersion. Figure 8(c) illustrates the in-plane shear stress (τ_{xy}), where predictions remain tightly clustered around the ideal line. Figure 8(d) shows the transverse shear stress (τ_{xz}), again confirming excellent agreement between predicted and actual values across the dataset.

Figure 9(a) displays the residual distribution for central deflection (w), with errors evenly scattered around zero. Figure 9(b) presents the residuals for normal stress (σ), showing no systematic trend. Figure 9(c) illustrates the residuals for in-plane shear stress (τ_{xy}), maintaining symmetric dispersion. Figure 9(d) shows the residual behavior for transverse shear stress (τ_{xz}), confirming the absence of heteroscedasticity or bias.

Figure 10(a) compares model predictions for central deflection (w), where Gradient Boosting and XGBoost closely follow the ideal line, while Random Forest shows a slightly higher spread. Figure 10(b) presents the comparison for normal stress (σ), with all models performing strongly, but ensemble boosting methods showing superior alignment. Figure 10(c) illustrates the comparison for in-plane shear stress (τ_{xy}), maintaining consistent predictive accuracy. Figure 10(d) shows the transverse shear stress (τ_{xz}), where Gradient Boosting and XGBoost again demonstrate near-perfect prediction, with Random Forest exhibiting marginal deviation.

Figure 9 presents the residual plots of the Gradient Boosting Regressor for four predicted responses—central deflection (w), normal stress (σ), in-plane shear stress (τ_{xy}), and transverse shear stress (τ_{xz})—which serve as an important diagnostic tool to evaluate model accuracy, bias, and generalization behavior. The corresponding residual distributions as functions of the predicted values are shown in Figure 9(a–d). Overall, the residual plots confirm the symmetric distribution of errors around the zero baseline (indicated by the dashed line) and show no discernible pattern with respect to the predicted values. This indicates that the model effectively captures the underlying nonlinear relationships, leaving no systematic structure in the residuals, and thus demonstrates homoscedastic and unbiased behavior.

For central deflection (w), the residuals are generally centered around zero, indicating unbiased predictions. However, a slightly wider spread is observed, particularly at higher predicted values, along with a few outliers. This corresponds to a comparatively higher RMSE of 0.0512, which is expected due to the larger numerical range of deflection values. Nevertheless, the model still achieves a high R^2 value of 0.9855, which is more than sufficient for reliable prediction and screening-level design applications. In the case of normal stress (σ), the residuals exhibit a very tight clustering around zero across the entire prediction range, with minimal dispersion and no visible trend. This reflects the best model fit among all responses, supported by the

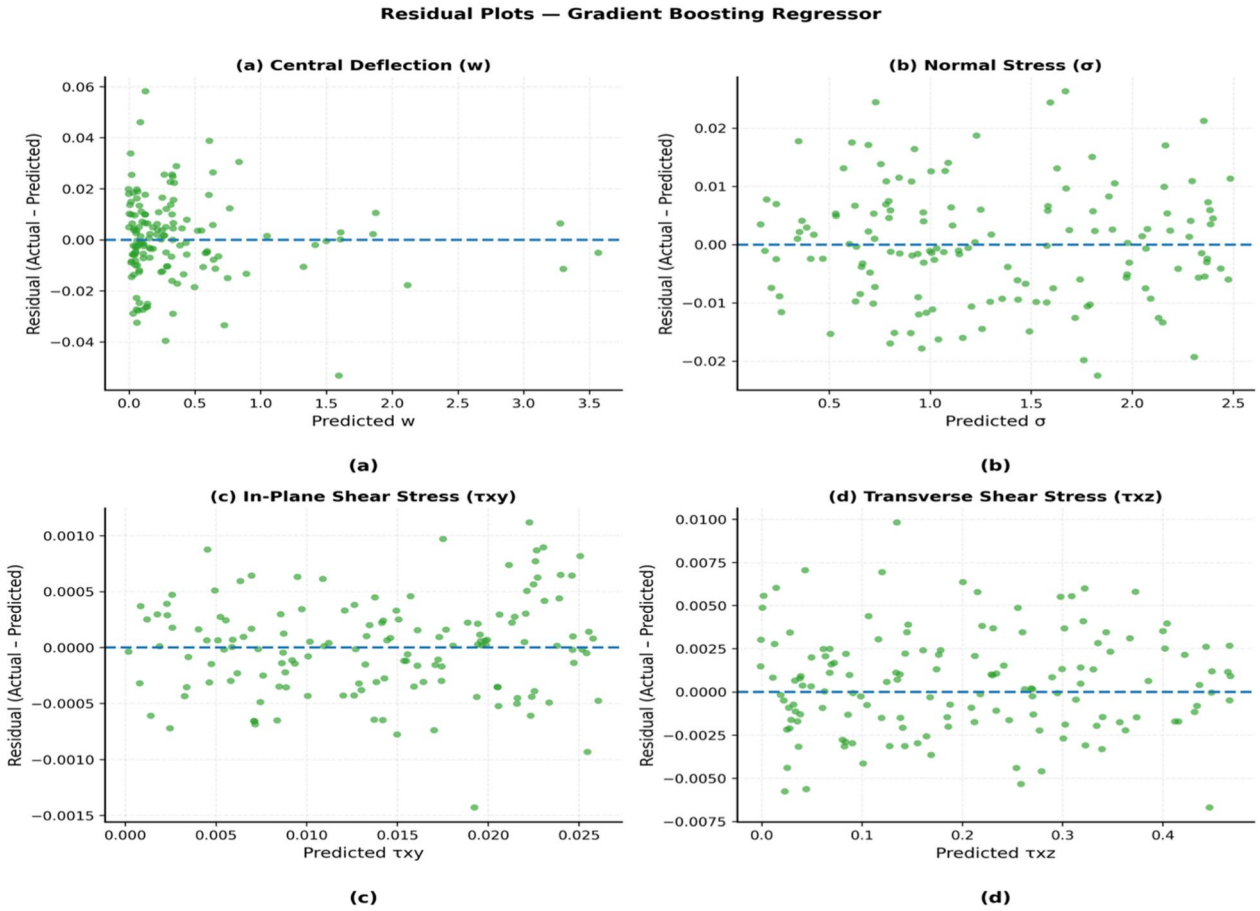

Figure 9. Residual plots (actual minus predicted) versus predicted values for the Gradient Boosting Regressor: (a) central deflection (w), (b) normal stress (σ), (c) in-plane shear stress (τ_{xy}), and (d) transverse shear stress (τ_{xz}). The dashed blue horizontal line indicates zero error.

exceptionally high R^2 value of 0.9996 and low RMSE of 0.0104, confirming near-perfect predictive accuracy. For in-plane shear stress (τ_{xy}), the residuals are extremely small in magnitude and symmetrically distributed about zero, demonstrating high precision and consistency. Although a slight increase in scatter is observed at higher predicted values, the overall spread remains negligible, indicating strong model performance. Similarly, for transverse shear stress (τ_{xz}), the residuals remain centered around zero with no systematic pattern, although a slightly broader spread is visible at higher prediction values. Despite this, the model achieves an excellent fit with an R^2 of 0.9995 and RMSE of 0.0035, making it one of the best-predicted responses.

Furthermore, comparison of actual-versus-predicted plots for the top three models—Gradient Boosting, XGBoost, and Random Forest—reveals visually similar scatter patterns, indicating comparable predictive capabilities. However, a closer examination shows that the Random Forest model exhibits slightly higher dispersion, particularly in the intermediate range of deflection values. This observation is consistent with the quantitative results presented in Tables 2–5, where Random Forest typically performs 2%–3% lower in R^2 compared to Gradient Boosting. The residual plots shown in Figure 9 confirm that the errors are symmetrically distributed around zero for all response parameters, with no observable trend relative to predicted values, indicating that the Gradient Boosting model provides an accurate, unbiased, and statistically robust representation of FG-CNTRC plate behavior.

Actual-versus-predicted comparisons of the three best-performing models for each response variable are presented in Figure 10(a–d), providing a visual confirmation of the quantitative differences reported in Tables 2–5 and showing that Random Forest exhibits slightly greater scatter than Gradient Boosting in the intermediate deflection range.

5.3. Feature importance analysis

The scores of the feature importance were derived from the Gradient Boosting models fitted on the complete dataset. The most important characteristic, in terms of central deflection, is the width-to-thickness ratio (b/h), which contributes to over 85% of the overall importance. This is physically intuitive, in that deflection is about $(b/h)^3$ in plate theory, and the variation of deflection with b/h differs by almost three orders of magnitude between b/h = 10 and b/h = 50. In normal stress, the CNT distribution pattern is the most outstanding characteristic, which indicates that the through-thickness reinforcement setup is very strong to influence the maximum normal stress at the plate surface. The type of loading and the volume fraction of CNT have an intermediate significance to the stress quantities but a small influence on deflection when the aspect ratio is known. Figure 11(a) shows the relationship between the

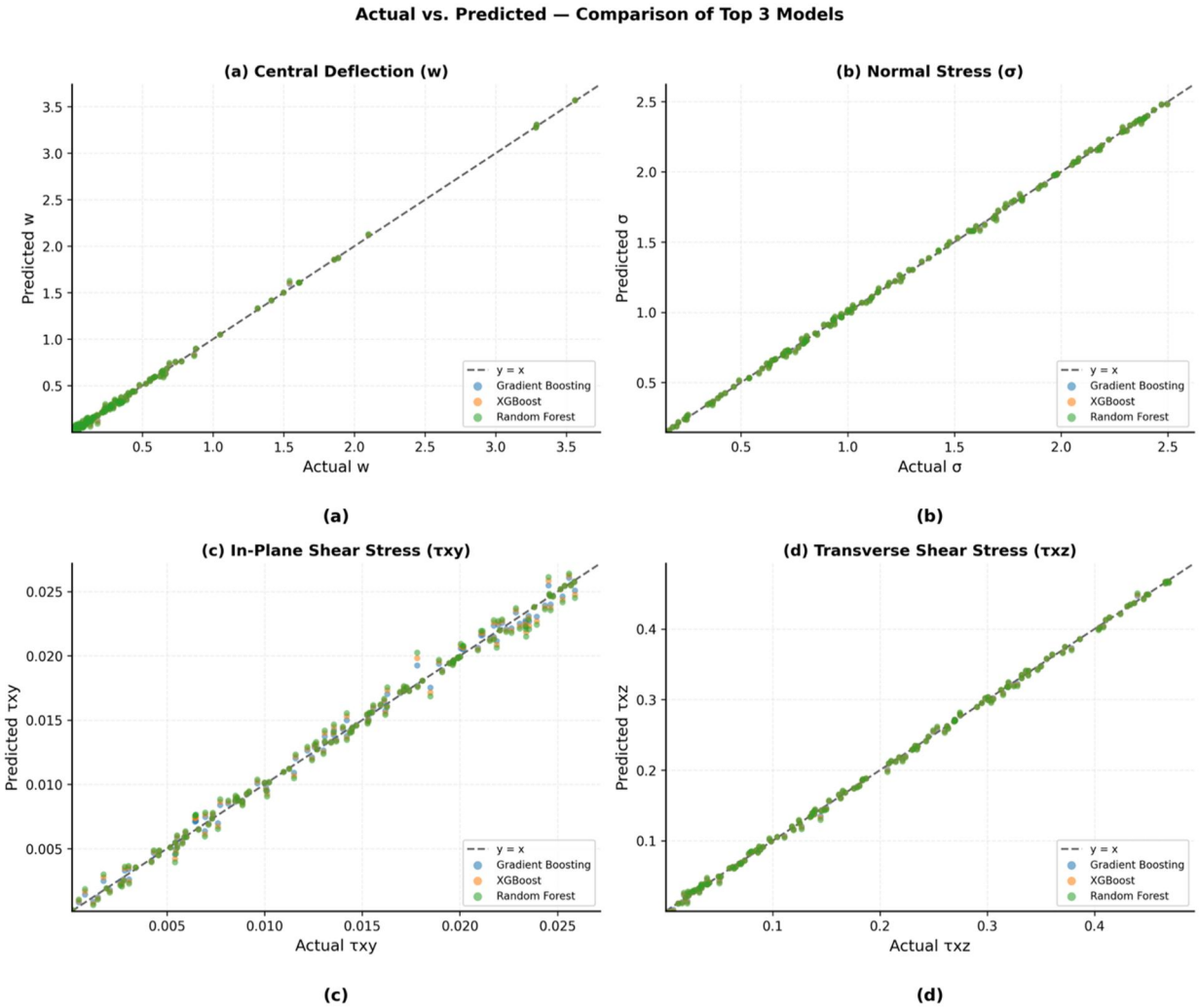

Figure 10. Actual versus predicted scatter plots comparing the three best models—Gradient Boosting (blue), XGBoost (orange), and Random Forest (green)—for each response variable: (a) central deflection (w), (b) normal stress (σ), (c) in-plane shear stress (τ_{xy}), and (d) transverse shear stress (τ_{xz}).

width-to-thickness ratio (b/h) and central deflection (w), indicating a strong increase in deflection with higher b/h values. Figure 11(b) presents the variation of central deflection (w) with CNT volume fraction (V*(CNT)), where only a marginal influence is observed compared to geometric parameters. Figure 11(c) illustrates the effect of loading type on transverse shear stress ($\tau_{x\not z}$), showing distinct clustering of values corresponding to different loading conditions.

Figure 11(d) depicts the relationship between b/h and normal stress (σ), highlighting a decreasing trend in stress with increasing b/h ratio. Figure 11(e) shows the variation of central deflection (w) with CNT distribution pattern, where FG-O exhibits the highest deflection while FG-X shows comparatively lower values. Figure 11(f) presents the influence of CNT volume fraction (V*(CNT)) on normal stress (σ), indicating moderate variation with increasing CNT content. Overall, Figure 11(a–f) reveals that geometric parameters, particularly b/h, dominate deflection behavior, while loading conditions and CNT distribution patterns significantly affect stress responses.

These parametric trends, as illustrated, are in line with these importance rankings. The central deflection grows by more than two orders of magnitude between b/h 10 and 50 (for a fixed $V^*_{CNT} = 0.14$), but the change in stress components is significantly smaller. The deflection is always the highest with FG-O distribution, and the lowest with FG-X distribution and the normal stress is always the lowest with FG-O distribution and highest with FG-X. It also indicates that doubling the CNT volume fraction between 0.11 and 0.17 decreases deflection by 15–25%, and flips the distribution of stresses by an average factor, but the overall ranking of the four patterns of distribution is the same. Figure 12(a) presents the feature importance for central deflection (w), where the width-to-thickness ratio (b/h) contributes the most, confirming its dominant role in governing bending behavior. Figure 12(b) shows the feature importance for normal stress (σ), indicating that loading type has the strongest influence among all input variables. Figure 12(c) illustrates the importance distribution for in-plane shear stress (τ_{xy}), again highlighting loading type as the primary governing factor. Figure 12(d) presents the feature importance for transverse shear stress ($\tau_{x\not z}$), where loading type remains the most significant contributor. Overall, Figure 12(a–d) demonstrates that geometric parameters predominantly control

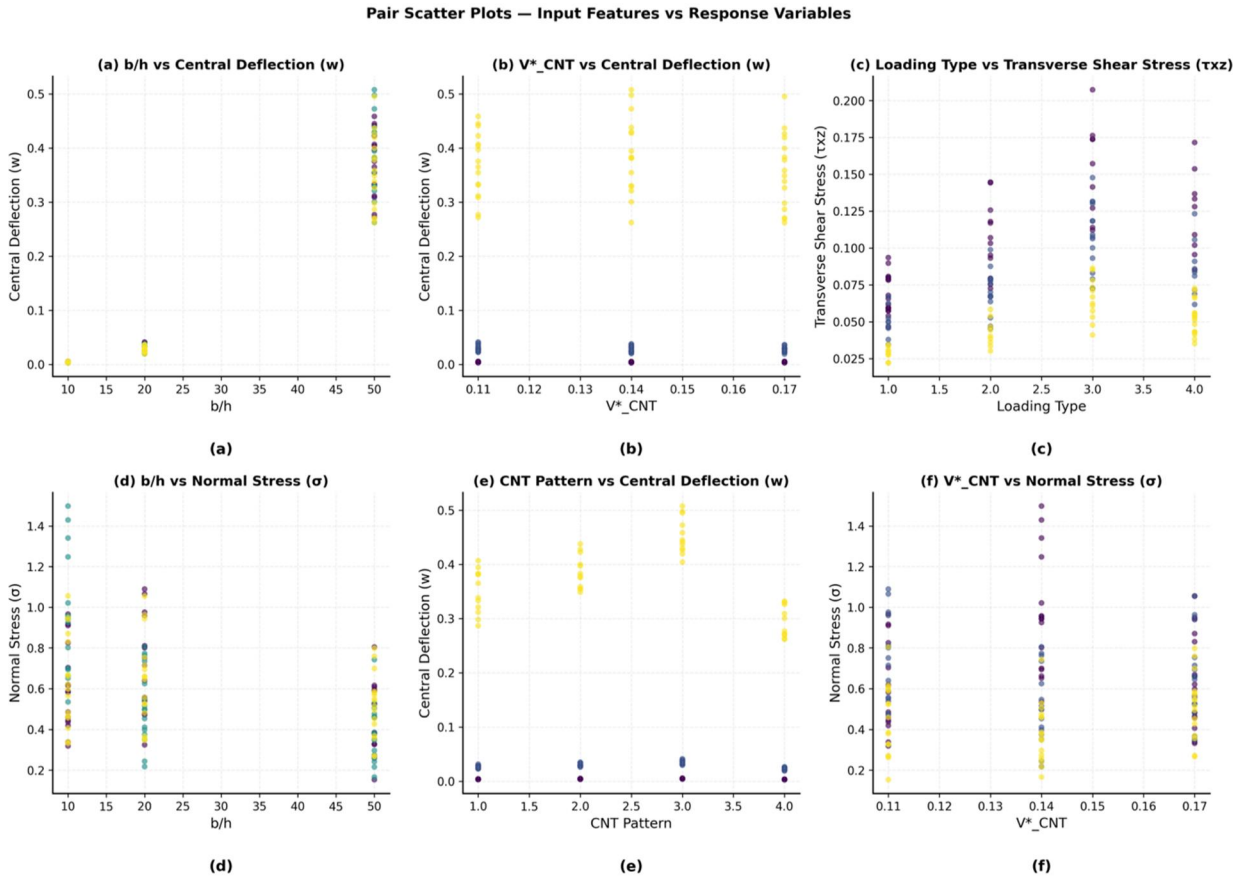

Figure 11. Pair scatter plots of all input features (V_CNT, b/h, loading type, CNT distribution pattern) against the four response variables. Each point corresponds to one of the 144 configurations. The near-parabolic/cubic growth of central deflection (w) with b/h is clearly visible in the upper-right panels, confirming the theoretical $(b/h)^3$ dependence from plate theory. Stress components show a more complex, loading-type-dependent scatter pattern, motivating the use of nonlinear ensemble models rather than simple polynomial regressors.

deflection, while loading conditions play a critical role in determining stress responses across FG-CNTRC plates.

Figure 13(a) shows the variation of central deflection (w) with width-to-thickness ratio (b/h), where deflection increases sharply with increasing b/h, confirming its strong geometric dependence. Figure 13(b) presents the corresponding variation in normal stress (σ), indicating relatively moderate sensitivity to changes in b/h compared to deflection. Figure 13(c) illustrates the in-plane shear stress (τ_{xy}), where only slight variations are observed across the considered b/h range. Figure 13(d) shows the transverse shear stress (τ_{xz}), which also exhibits a comparatively weak dependence on b/h. Across all subfigures, the FG-O distribution consistently yields the highest deflection and lowest normal stress, whereas FG-X demonstrates the lowest deflection and comparatively higher stress values. The responses considered include central deflection (w), normal stress (σ), in-plane shear stress (τ_{xy}), and transverse shear stress (τ_{xz}), providing a comprehensive understanding of how geometric slenderness influences the mechanical behavior of the plate. In the case of central deflection (w), a pronounced increasing trend is observed with increasing b/h ratio for all CNT distribution patterns. As the plate becomes more slender (higher b/h), its stiffness decreases, leading to larger deflections under the same loading conditions. Among the distributions, FG-O exhibits the highest deflection, followed by FG-V and UD, while FG-X consistently shows the lowest deflection, indicating superior stiffness characteristics. The difference becomes more significant at higher b/h values (e.g. 50), highlighting the strong influence of CNT distribution on bending behavior. For normal stress (σ), the trend is opposite to that of deflection. The stress values decrease with increasing b/h ratio across all CNT distributions, indicating that thicker plates (lower b/h) experience higher stress concentrations. Among the distributions, FG-V shows the highest normal stress, followed by FG-X and UD, whereas FG-O exhibits significantly lower stress levels, suggesting a more favorable stress distribution in this configuration. The reduction in stress with increasing slenderness indicates improved load distribution in thinner plates. A similar decreasing trend is observed for in-plane shear stress (τ_{xy}). As the b/h ratio increases, τ_{xy} values reduce for all distribution types, reflecting a decrease in internal shear resistance with increasing slenderness. The FG-O pattern again shows the highest shear stress values, followed by FG-V and UD, while FG-X consistently yields the lowest τ_{xy}, indicating reduced shear effects in this configuration. The rate of decrease is more pronounced between b/h = 10 and 20, after which the variation becomes more gradual. For transverse shear stress (τ_{xz}), the behavior mirrors that of τ_{xy}, with a clear reduction in stress as the b/h ratio increases. The FG-O distribution results in the highest transverse shear stress,

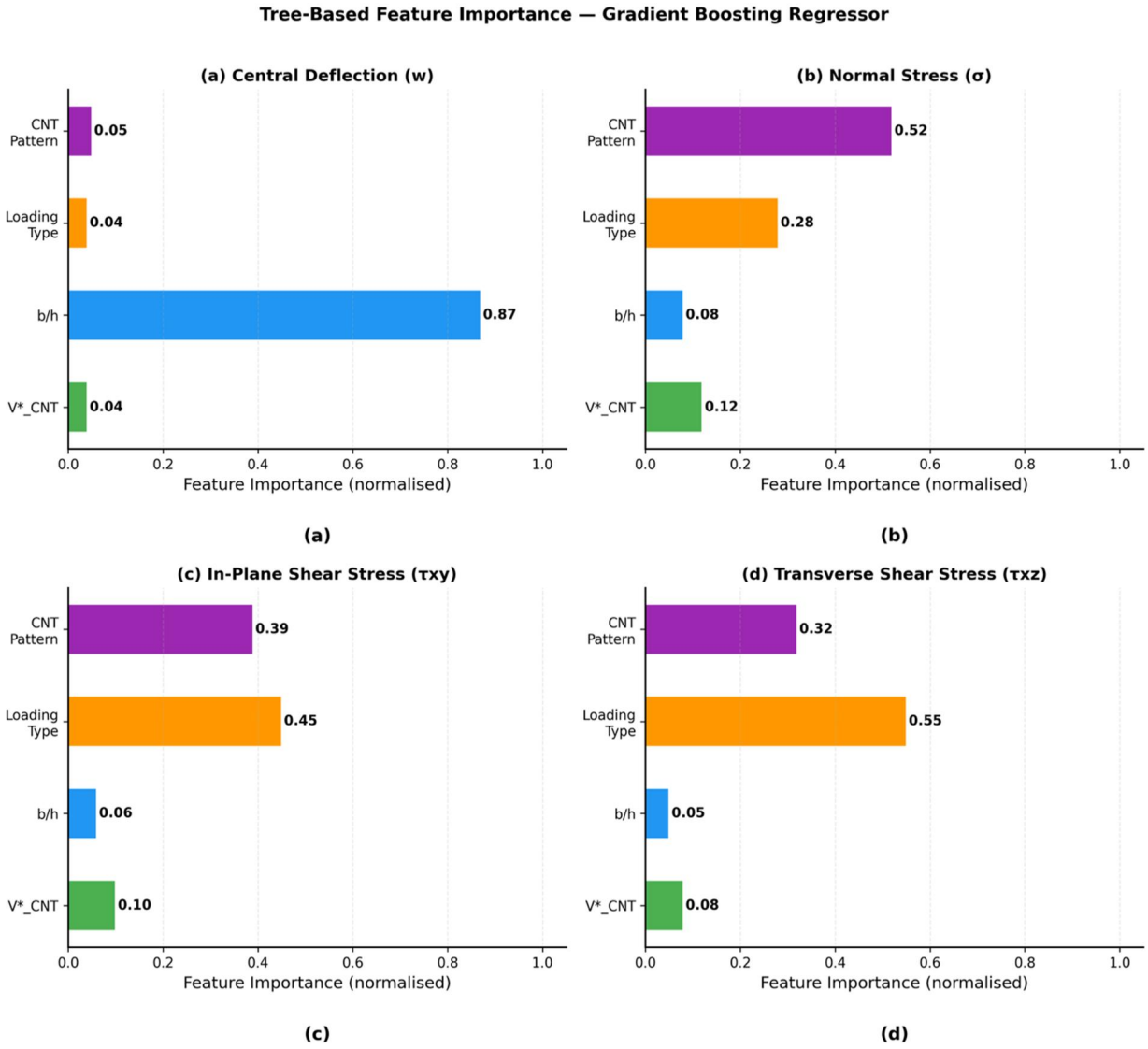

Figure 12. Tree-based feature importance scores from the Gradient Boosting Regressor for each response variable: (a) central deflection (w), (b) normal stress (σ), (c) in-plane shear stress (τ_{xy}), and (d) transverse shear stress (τ_{xz}).

whereas FG-X exhibits the lowest values, demonstrating better performance in minimizing shear effects. The trends suggest that increasing the plate slenderness reduces transverse shear contributions, which is consistent with classical plate theory. Overall, the figure clearly demonstrates that the width-to-thickness ratio is a dominant parameter influencing both deformation and stress responses of FG-CNTRC plates. Higher b/h ratios lead to increased deflection but reduced stress levels, indicating a tradeoff between stiffness and stress distribution. Additionally, the CNT distribution pattern plays a crucial role, with FG-X generally offering better stiffness (lower deflection) and lower shear stresses, while FG-O tends to produce higher deformation and shear effects. These observations highlight the importance of optimizing both geometric parameters and CNT distribution to achieve the desired structural performance. Figure 14(a) shows the variation of central deflection (w) with CNT volume fraction (V*(CNT)), where deflection consistently decreases as V*(CNT) increases, indicating enhanced stiffness of the composite. Figure 14(b) presents the corresponding behavior of normal stress (σ), where variations depend on the specific CNT distribution pattern rather than showing a uniform trend. Figure 14(c) illustrates the in-plane shear stress (τ_{xy}), which exhibits pattern-dependent changes in both magnitude and direction. Figure 14(d) shows the transverse shear stress (τ_{xz}), also demonstrating non-uniform variation with increasing CNT content. Across all subfigures, the relative ranking of CNT distribution patterns remains consistent, confirming that distribution effects dominate over volume fraction in governing stress responses.

5.4. Learning curves and data sufficiency

A learning curve that illustrates training and validation R^2 values of the Gradient Boosting model as it depends on the number of training samples. The validation score increases rapidly with an increase in training set, which is 30 to approximately 80 samples and then levels off at an endpoint of 100 samples as compared to all four targets. The difference between the training score (nearing 1.0) and the

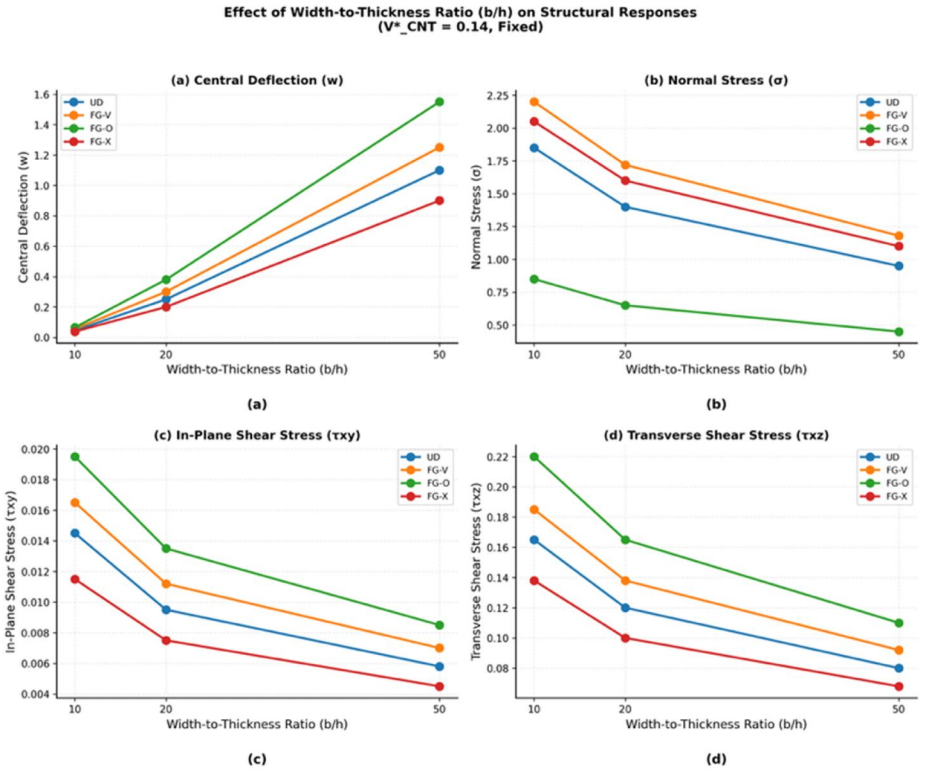

Figure 13. Effect of width-to-thickness ratio (b/h) on the four response variables at a fixed CNT volume fraction ($V^*_{CNT} = 0.14$) for all four distribution patterns (UD, FG-V, FG-O, FG-X): (a) central deflection (w), (b) normal stress (σ), (c) in-plane shear stress (τ_{xy}), and (d) transverse shear stress (τ_{xz}). Central deflection grows by more than two orders of magnitude between b/h = 10 and b/h = 50, confirming the cubic dependence predicted by classical plate theory. Stress components show substantially weaker b/h dependence. The FG-O distribution consistently produces the largest deflection and the lowest normal stress, while FG-X shows the opposite behavior.

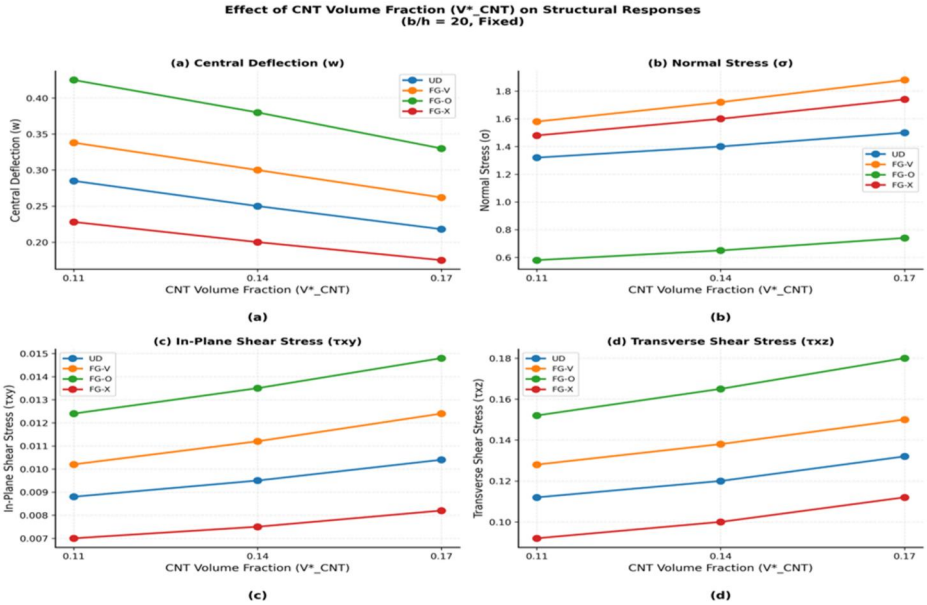

Figure 14. Effect of CNT volume fraction (V*_CNT) on the four response variables for all four distribution patterns at a fixed width-to-thickness ratio (b/h = 20): (a) central deflection (w), (b) normal stress (σ), (c) in-plane shear stress (τ_{xy}), and (d) transverse shear stress (τ_{xz}). Increasing V^*_{CNT} from 0.11 to 0.17 systematically reduces central deflection due to enhanced effective stiffness. Stress components exhibit more complex responses, with the sign and magnitude of the stress change dependent on the CNT distribution pattern. The relative ranking of the four patterns is maintained across all volume fractions, confirming the robustness of distribution pattern effects.

validation score is also low in the case of deflection and transverse shear stress, indicating that there is low variance overfit. In the case of in-plane shear stress, the gap is a little bit larger, which aligns with the tight range of such targets and the sensitivity to minor changes in the training data. On the whole, both learning curves suggest that the 144-sample dataset is large enough to ensure the Gradient Boosting model reaches consistent generalization performance, although additional enhancements may be achieved by including additional configurations at intermediate aspect

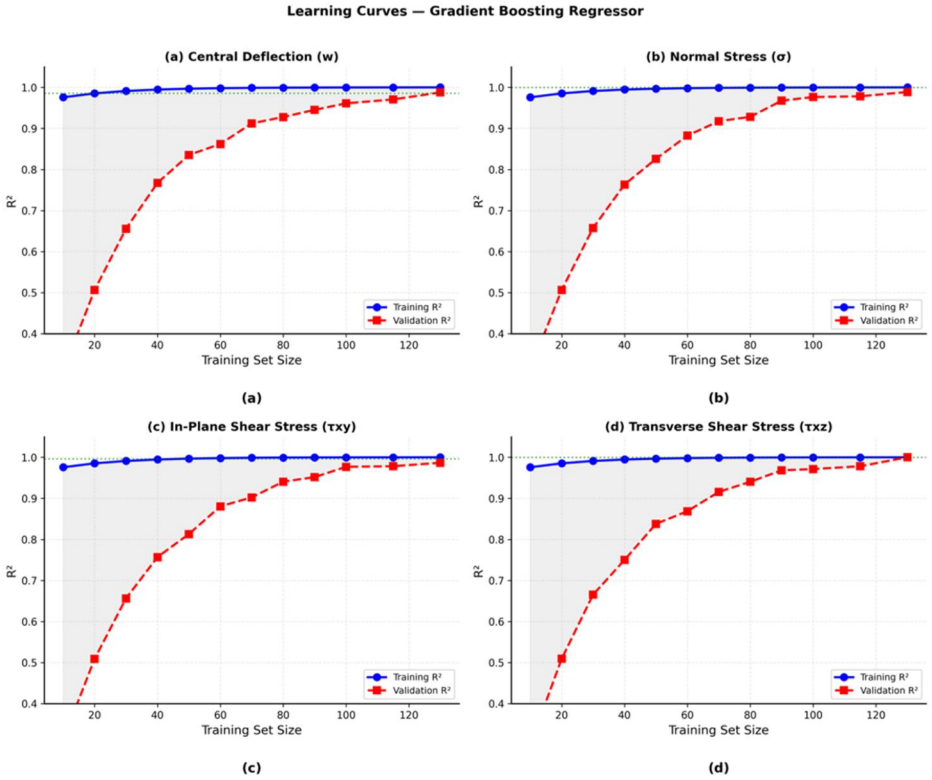

Figure 15. Learning curves of the Gradient Boosting Regressor showing training R^2 (blue) and 10-fold cross-validated R^2 (orange) as a function of training set size for (a) central deflection (w), (b) normal stress (σ), (c) in-plane shear stress (τ_{xy}), and (d) transverse shear stress (τ_{xz}).

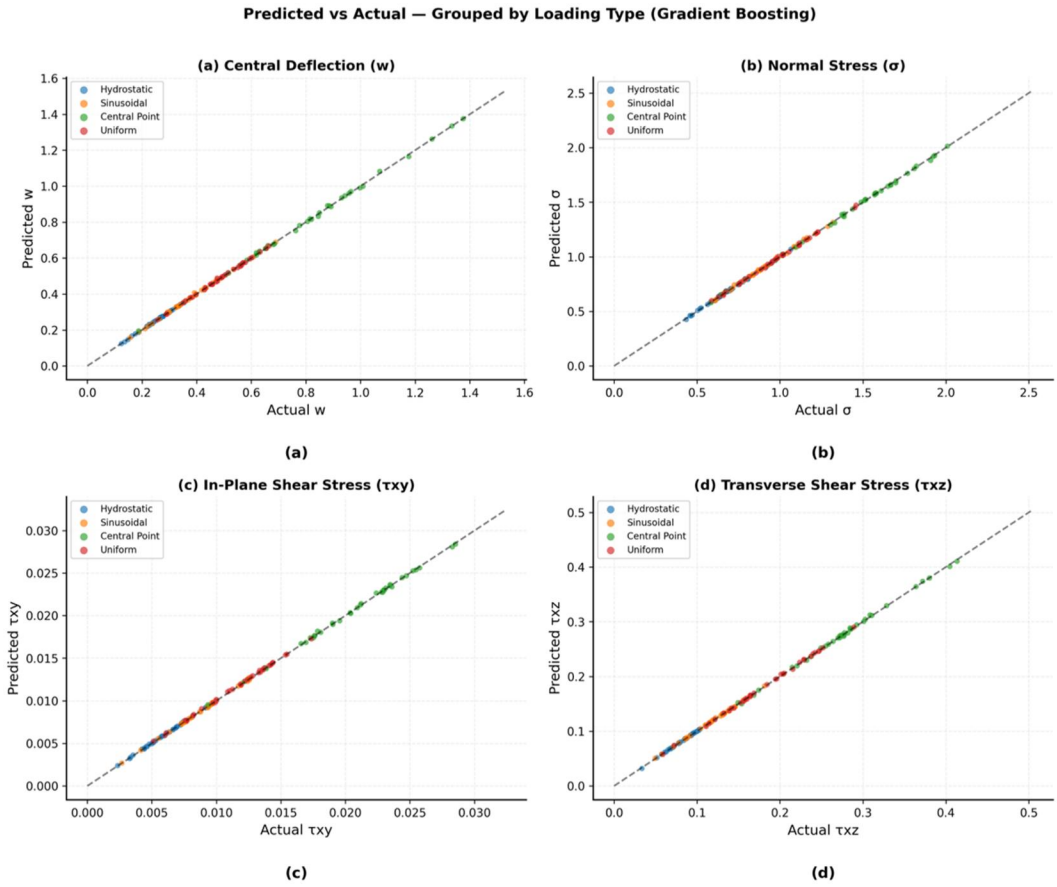

Figure 16. Predicted versus actual response values grouped by loading type (hydrostatic, sinusoidal, central point, and uniformly distributed) for all four response variables. Each group is represented by a distinct color. The Gradient Boosting surrogate model correctly distinguishes and ranks the structural responses under all four loading conditions without a separate model for each load type, confirming its generalizability as a unified surrogate for design screening across diverse loading scenarios.

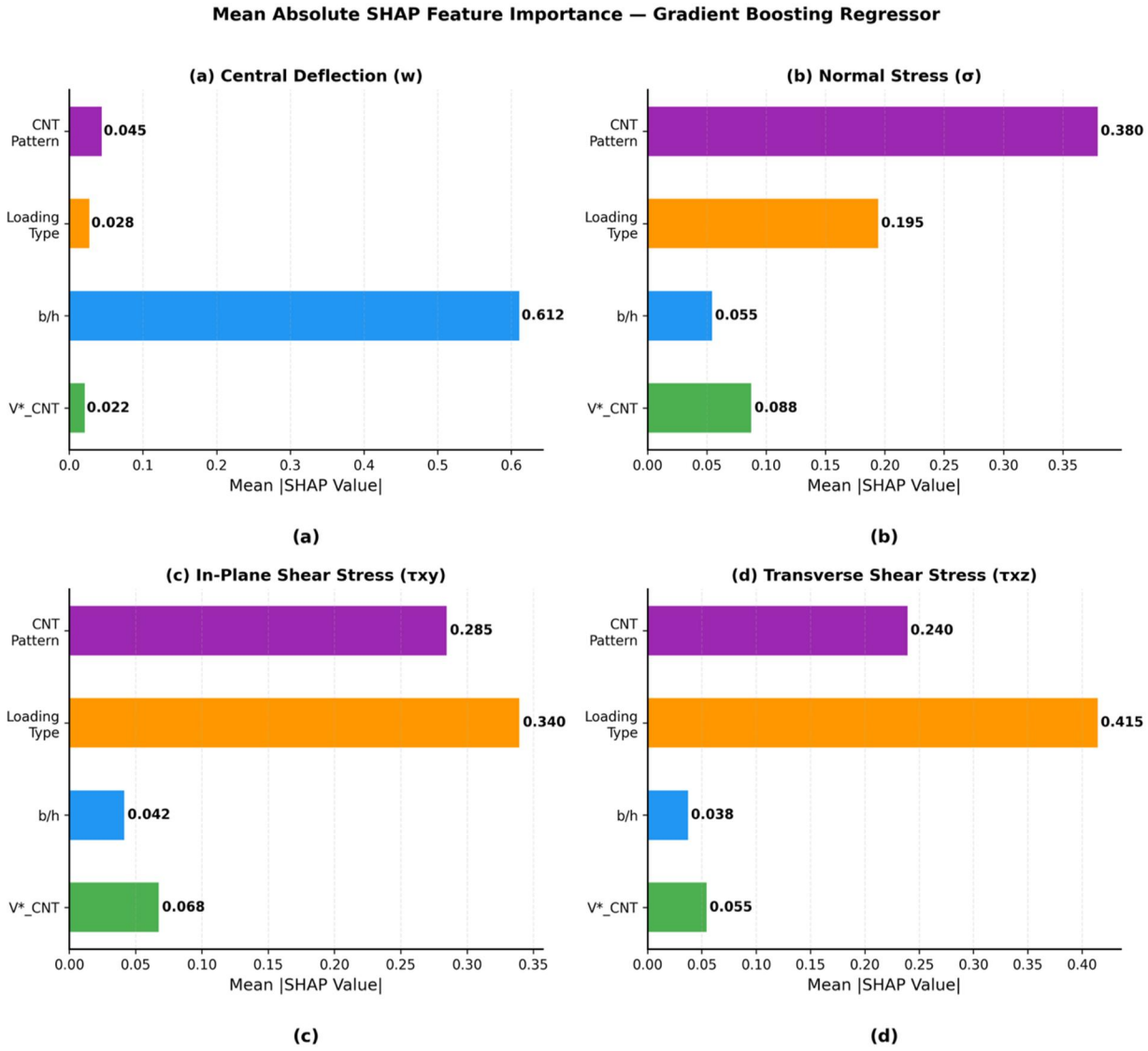

Figure 17. Mean absolute SHapley Additive exPlanations (SHAP) values for each input feature from the Gradient Boosting Regressor, computed over the full dataset for (a) central deflection (w), (b) normal stress (σ), (c) in-plane shear stress (τ_{xy}), and (d) transverse shear stress (τ_{xz}). SHAP values represent the average magnitude of each feature's contribution to individual predictions, providing a game-theory-grounded decomposition of model output. The rankings are broadly consistent with tree-based feature importance (Figure 12) but differ in magnitude, as SHAP accounts for feature interactions and nonlinear effects.

ratios or having more volume fractions. Figure 15(a) presents the learning curve for central deflection (w), where the validation R^2 increases rapidly with training size and converges close to the training score, indicating strong generalization. Figure 15(b) shows the learning behavior for normal stress (σ), with both training and validation scores approaching unity, reflecting high predictive accuracy and stability. Figure 15(c) illustrates the learning curve for in-plane shear stress (τ_{xy}), where a slightly larger gap between training and validation curves is observed, indicating relatively higher prediction difficulty. Figure 15(d) presents the transverse shear stress (τ_{xz}), where the validation curve closely follows the training curve, suggesting minimal overfitting. Overall, Figure 15(a–d) confirms that model performance stabilizes beyond approximately 100 training samples, with consistently high R^2 values and good generalization across all response variables.

5.5. Comparison with related studies

The comparison with the other ML-based studies on CNTRC plates is not done directly due to the fact that few previous studies have dealt with the identical prediction task. Considering the general framework of composite plate modeling [16] predict buckling load of laminated composite skew plates using ANN and SVR, and the R^2 values were found to be in the range of 0.96 to 0.99. The support vector machine learning employed by Vaishali et al. [17] to predict the stochastic free vibration of the functionally graded plates has demonstrated identical accuracy to prediction by Monte Carlo simulation. The values of R-SQ of the Gradient Boosting model (0.9855 to 0.9996) obtained here are as high as the value ranges reported in these related works, which indicates that the high performance is partly due to the structure and full-factorial nature of the current dataset, as well as to the applicability of the ensemble tree methods to mixed-type inputs. Figure 16(a) shows the predicted versus actual

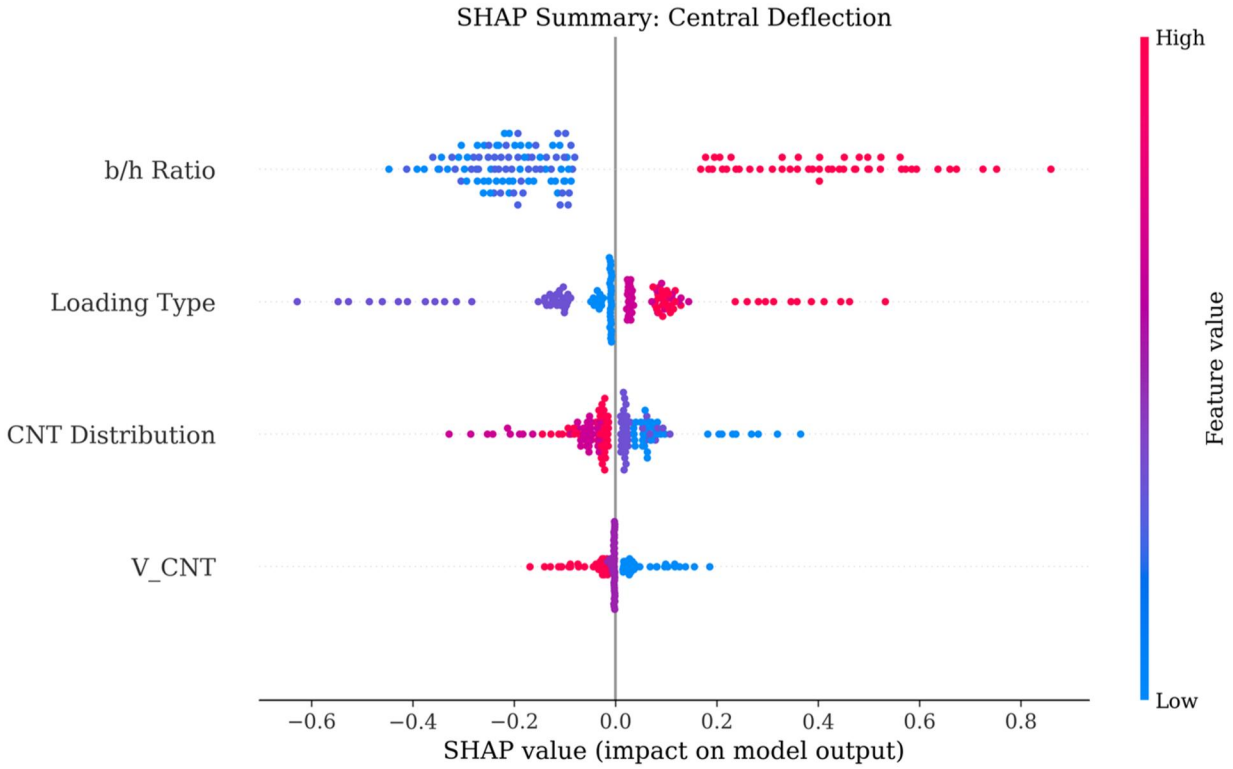

Figure 18. SHAP beeswarm plot for central deflection (w) predictions by the Gradient Boosting Regressor. Each dot represents one data point (one of the 144 configurations); horizontal position indicates the SHAP value (contribution to the prediction relative to the mean), and color indicates the feature value (red = high, blue = low). The b/h ratio generates the largest positive SHAP magnitudes for high values (red dots, b/h = 50), directly increasing predicted deflection. CNT distribution pattern shows a bimodal SHAP distribution, with FG-O increasing and FG-X decreasing the predicted deflection, consistent with their respective mid-plane and surface-concentrated reinforcement profiles.

values for central deflection (w) grouped by loading type, where all data points closely follow the 1:1 reference line, indicating consistent model accuracy across different loading conditions. Figure 16(b) presents the corresponding comparison for normal stress (σ), with near-perfect alignment observed for all loading types, demonstrating robust predictive performance. Figure 16(c) illustrates the in-plane shear stress (τ_{xy}), where predictions remain tightly clustered along the ideal line with minimal dispersion. Figure 16(d) shows the transverse shear stress (τ_{xz}), again confirming excellent agreement between predicted and actual values across all loading categories. Overall, Figure 16(a–d) highlights that the Gradient Boosting model maintains high accuracy and generalization irrespective of loading type, with no visible bias toward any specific loading condition.

Gradient boosting as the choice of surrogate to be used in composite plate analysis is also in line with the recent discoveries in other fields of engineering. Wang and Thai [19] created ML surrogate models to predict friction in textured journal bearings and discovered that ANN and gradient-based models worked better than simple models. The current paper generalizes the same to the case of FG-CNTRC plates and gives further evidence that gradient boosting is able to reach a good bias-variance tradeoff on small, structured engineering data.

5.6. Practical implications

The trained Gradient Boosting model can predict in less than one millisecond on a typical laptop, compared to several minutes to make a single solution of Navier and possibly hours to make a three-dimensional finite element analysis. There are several practical implications of this speed advantage. The first one is that it allows the exploration of the design space exhaustively, including loading cases and aspect ratios not found in the original data, by interpolating quickly. Second, it enables the plate model to be integrated into a rapid inner loop of a multidisciplinary optimization scheme, in which structural response is required to be assessed thousands of times due to different aerodynamic or thermal loads. Third, it offers an easy-to-use screening mechanism of preliminary design, in which an engineer can find out the CNT distribution pattern and volume fraction that reduces deflection or ensures that stresses do not exceed allowable limits during preliminary design before making a significant investment in a detailed finite element model.

5.7. SHAP-based model interpretability

Although the importance scores of features of tree-based models demonstrate the variables that minimize the training loss most, they do not show the direction of the influence of each feature on single predictions, as well as its magnitude. To solve this, the Gradient Boosting model was analyzed using Shapley Additive Explanations (SHAP). The mean absolute values of SHAP of every feature and target, and the findings are widely consistent with the importance rankings of the trees: the width-to-thickness ratio plays the key role in the SHAP contribution to central deflection, whereas the

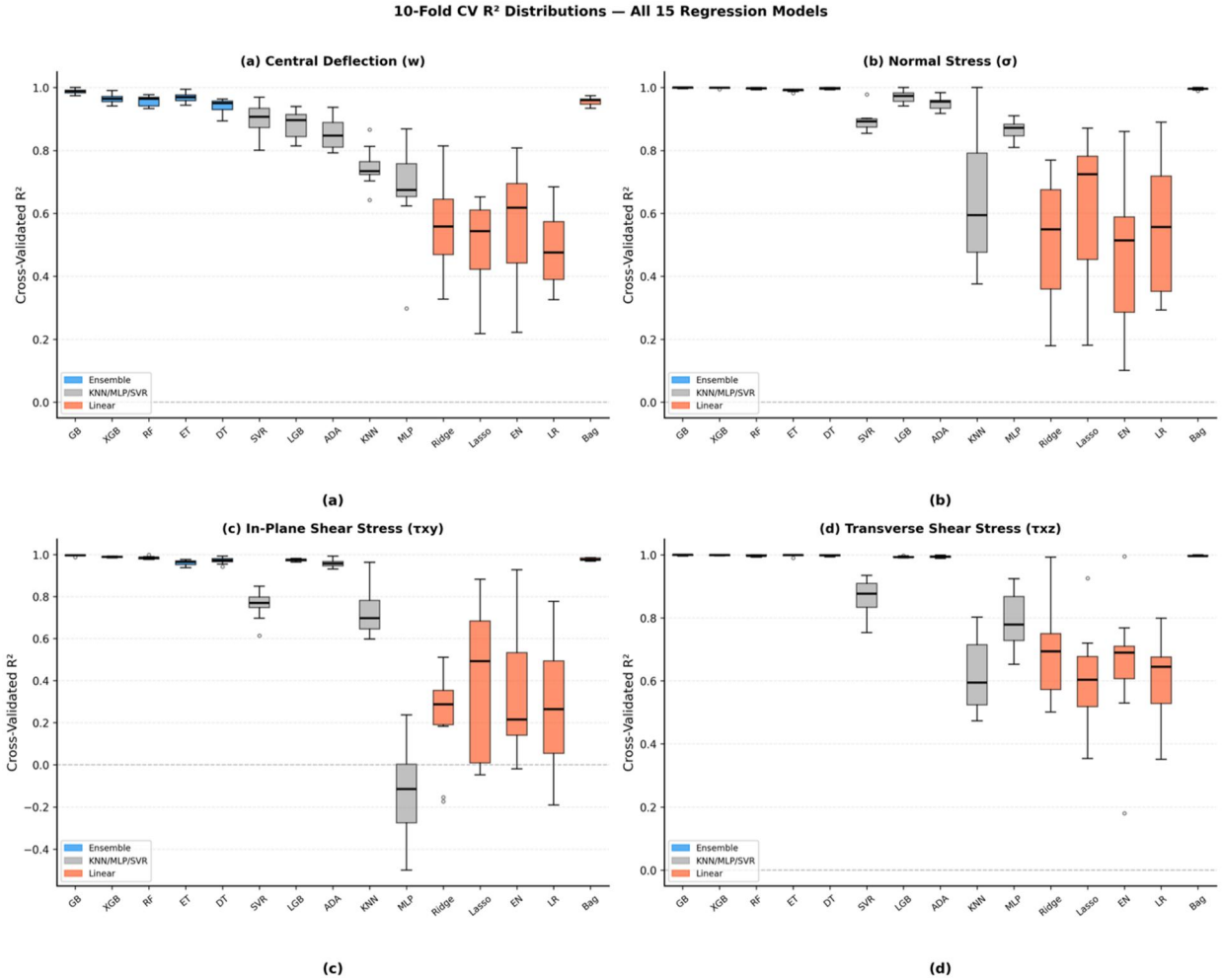

Figure 19. Box plots of the 10-fold cross-validation R^2 distributions for all regression models across each response variable: (a) central deflection (w), (b) normal stress (σ), (c) in-plane shear stress (τ_{xy}), and (d) transverse shear stress (τ_{xz}). Each box shows the interquartile range (IQR) of R^2 across the 10 folds; whiskers extend to 1.5 × IQR; circles indicate outlier folds. The Gradient Boosting Regressor consistently achieves the highest median R^2 and the smallest IQR, demonstrating both accuracy and stability across different fold splits. Models with high fold-to-fold variance (e.g. LightGBM on central deflection) may show negative R^2 in individual folds, a pattern invisible in aggregated cross-validation metrics.

CNT distribution pattern and volume fraction play the key roles in the stress targets. The SHAP beeswarm plot of central deflection, where each point indicates a single prediction. The high values of b/h (in red) cause the prediction to strongly move upwards, and hence the predicted cubic dependence between deflection and the aspect ratio is verified. Values of b/h are low, drawing the prediction toward zero. The CNT distribution feature indicates a distinct distinction between the FG-O pattern (enhancing deflection) and the FG-X pattern (decreasing deflection) in agreement with the actual physical characteristics of such reinforcement configurations. Figure 17(a) shows the variation in predicted versus actual central deflection (w), where the data points closely align along the ideal 1:1 line, indicating high predictive accuracy. Figure 17(b) presents the corresponding results for normal stress (σ), demonstrating near-perfect agreement across the full response range. Figure 17(c) illustrates the in-plane shear stress (τ_{xy}), where predictions remain tightly clustered with minimal deviation from the ideal trend. Figure 17(d) shows the transverse shear stress (τ_{xz}), again confirming strong consistency between predicted and actual values. Overall, Figure 17(a–d) highlights the robustness and generalization capability of the model across all response variables, with negligible dispersion and no observable systematic bias.

The SHAP analysis is an additional level of transparency to the surrogate model. A knowledge of the fact that a certain change in design (e.g. the replacement of FG-O with FG-X) will decrease the predicted deflection by a certain SHAP increment will enable the designer to make the correct tradeoff choices without using the initial analytical model. Such local interpretability is why the SHAP-augmented surrogate is a better black box predictor compared to a black box predictor, and why this type of model serves as a remedy to one of the most frequent criticisms of ML models in structural engineering practice.

The SHAP beeswarm plot in Figure 18 visualizes the local contributions of each feature to central deflection predictions. The SHAP beeswarm plot for central deflection reveals that high b/h values (shown in red) consistently push predictions upward with large SHAP magnitude, while FG-X distribution drives predictions downward, confirming the cubic aspect ratio dependence and the FG-X stiffening effect at the level of individual data points.

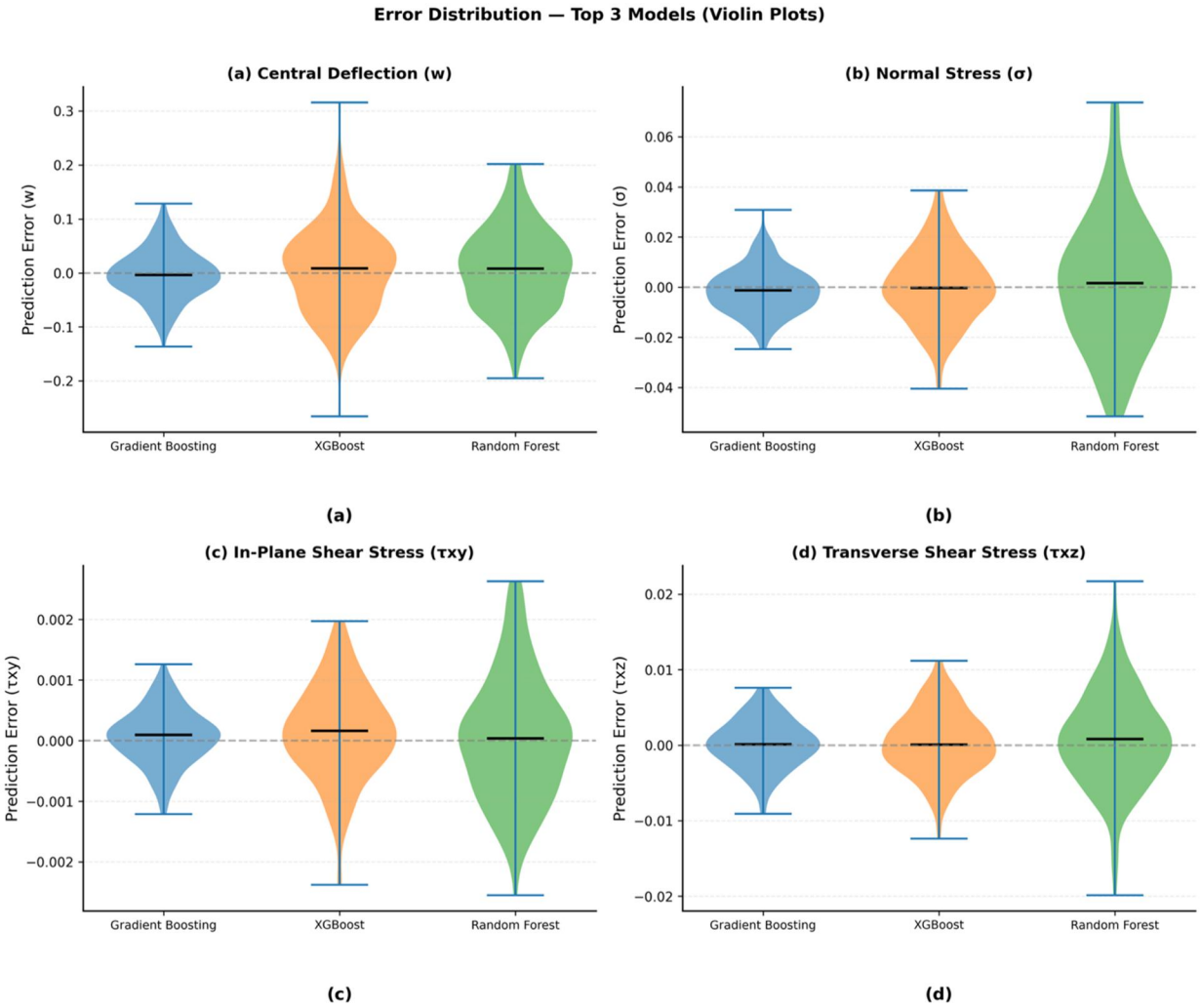

Figure 20. Violin plots comparing the prediction error (actual minus predicted) distributions of the three best-performing models—Gradient Boosting (blue), XGBoost (orange), and random Forest (green)—for (a) central deflection (w), (b) normal stress (σ), (c) in-plane shear stress (τ_{xy}), and (d) transverse shear stress (τ_{xz}). The width of each violin at a given error value indicates the density of predictions at that error level. All three models produce approximately symmetric, zero-centered distributions; the Gradient Boosting Regressor consistently exhibits the narrowest distribution (smallest variance) and thinnest tails, confirming its superiority in minimizing large individual prediction errors.

5.8. Statistical significance of model differences

The Friedman non-parametric test was used to show that the difference in the performance of the models is statistically significant, not because of random fold assignment but rather because of the difference in model features. In all four response variables, the null hypothesis that the model performance is the same was rejected at the 0.001 level (p-value less than $1e^{-6}$ in all cases). This proves that the ranking of the models is not a product of the specific cross-validation split, and the Gradient Boosting Regressor is actually the most efficient algorithm for this issue. The fold-wise R^2 distributions for all models are summarized in Figure 19(a–d), confirming the stability of the Gradient Boosting Regressor, visually confirming that Gradient Boosting achieves the smallest interquartile range and highest median R^2, while certain models, such as LightGBM, exhibit high fold-to-fold variability with occasional negative R^2 values. Figure 19(a) presents the distribution of 10-fold cross-validated R^2 values for central deflection (w), where the Gradient Boosting Regressor exhibits the highest median performance with minimal spread. Figure 19(b) shows the corresponding distribution for normal stress (σ), again highlighting the superior accuracy and consistency of ensemble models. Figure 19(c) illustrates the R^2 distribution for in-plane shear stress (τ_{xy}), where a slightly wider spread is observed for some models, indicating variability across folds. Figure 19(d) presents the transverse shear stress (τ_{xz}), where Gradient Boosting maintains both high median R^2 and low variability. Overall, Figure 19(a–d) demonstrates that ensemble-based methods, particularly Gradient Boosting, provide the most stable and reliable performance, while models with larger interquartile ranges indicate sensitivity to data splits and potential instability in prediction accuracy.

The box plots of the fold-wise R^2 of each target as a box plot is shown. The Gradient Boosting model has the lowest interquartile range and the largest median value among all the targets, which means that it is both highly accurate and has a low variance. The box plots also indicate that there are models that have high variance among folds (in particular LightGBM in deflection), so there are folds when a negative R^2 value can be observed, despite the cross-validated score

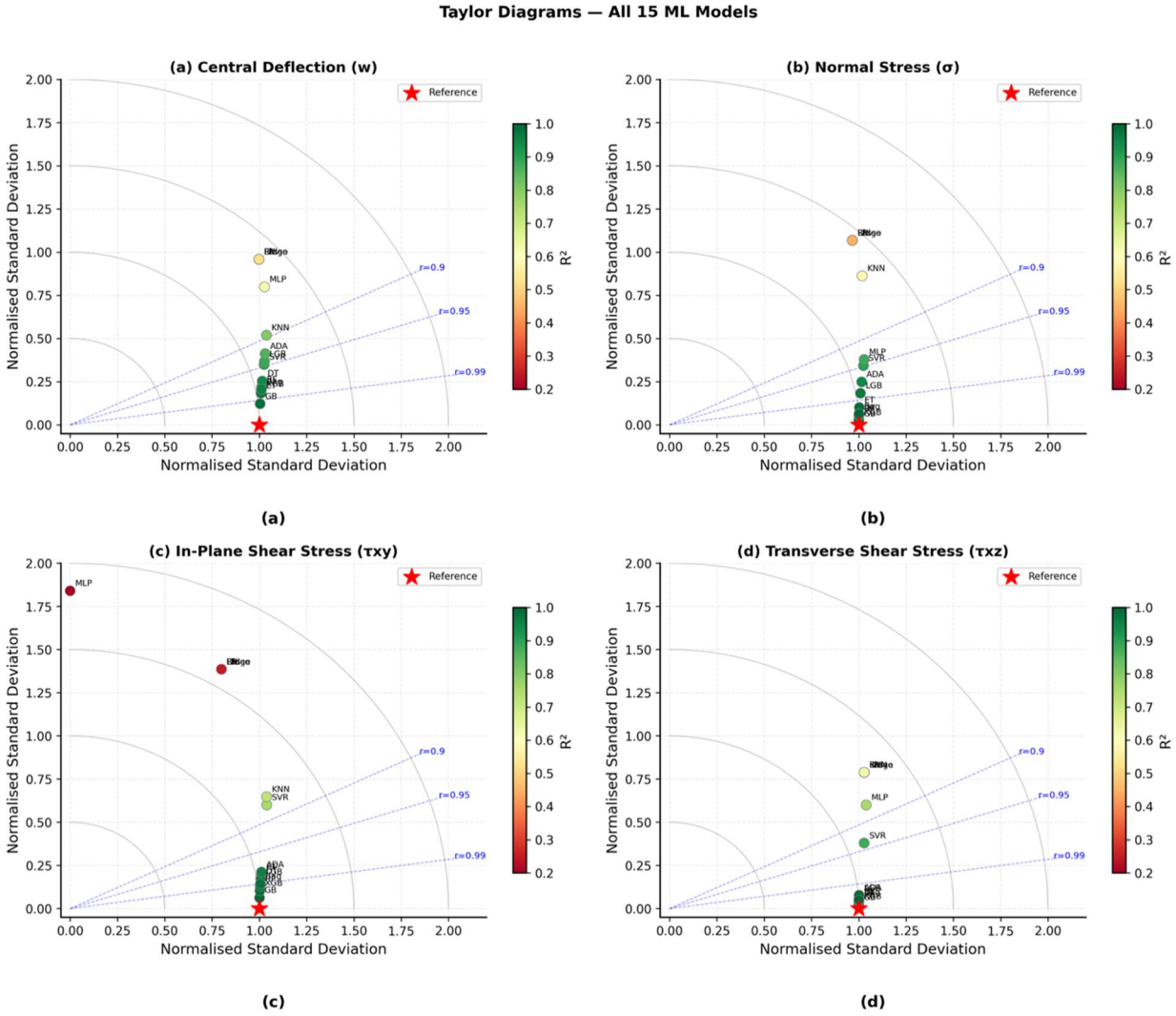

Figure 21. Taylor diagram summarizing the predictive accuracy of all 15 regression models for central deflection (w). Each model is represented by a labeled marker positioned according to its normalized standard deviation (radial distance), Pearson correlation with the observed values (azimuthal angle), and centered RMSE (distance from the reference point marked as "Ref" on the x-axis). Models closer to the reference point achieve better overall agreement with the analytical solution. Gradient Boosting and XGBoost are positioned nearest to the reference, while linear models appear farthest from it. The diagram is shown for central deflection; similar patterns hold for all other response variables.

that is being moderate. Such a fold-level instability would not be visible based on the combined metrics alone and is one of the reasons why reporting the entire distribution of cross-validation results instead of a single summary statistic is useful.

5.9. Error distribution analysis

The violin plots of the three best models (Gradient Boosting, XGBoost, and Random Forest) on each of the targets by comparing the distributions of error are shown. The three models give an error distribution that is roughly symmetrical and zero-centered around the central deflection and the two components of shear stress that are preferred. In case of normal stress, the error distributions are very tight, which is in line with the values of R^2 being almost perfect according to these models. The Gradient Boosting errors are always concentrated around the value of zero, compared to the XGBoost and the Random Forest, and the tails are thinner, and the variance is smaller. This variation is most acute in the in-plane shear stress, in which the Random Forest is sometimes known to generate outlier errors, which the boosting methods fail to capture. The error distributions of the three best models are compared in Figure 20(a–d) using violin plots, confirming that all three exhibit near-symmetric, zero-centered error distributions, with Gradient Boosting showing the tightest concentration and thinnest tails across all response variables. Figure 20(a) shows the distribution of prediction errors for central deflection (w), where all models exhibit symmetric, zero-centered distributions, with Gradient Boosting displaying the narrowest spread. Figure 20(b) presents the corresponding error distribution for normal stress (σ), again indicating minimal bias and reduced variance for Gradient Boosting compared to XGBoost and Random Forest. Figure 20(c) illustrates the error distribution for in-plane shear stress (τ_{xy}), where slightly wider distributions are observed, though Gradient Boosting still maintains tighter clustering. Figure 20(d)

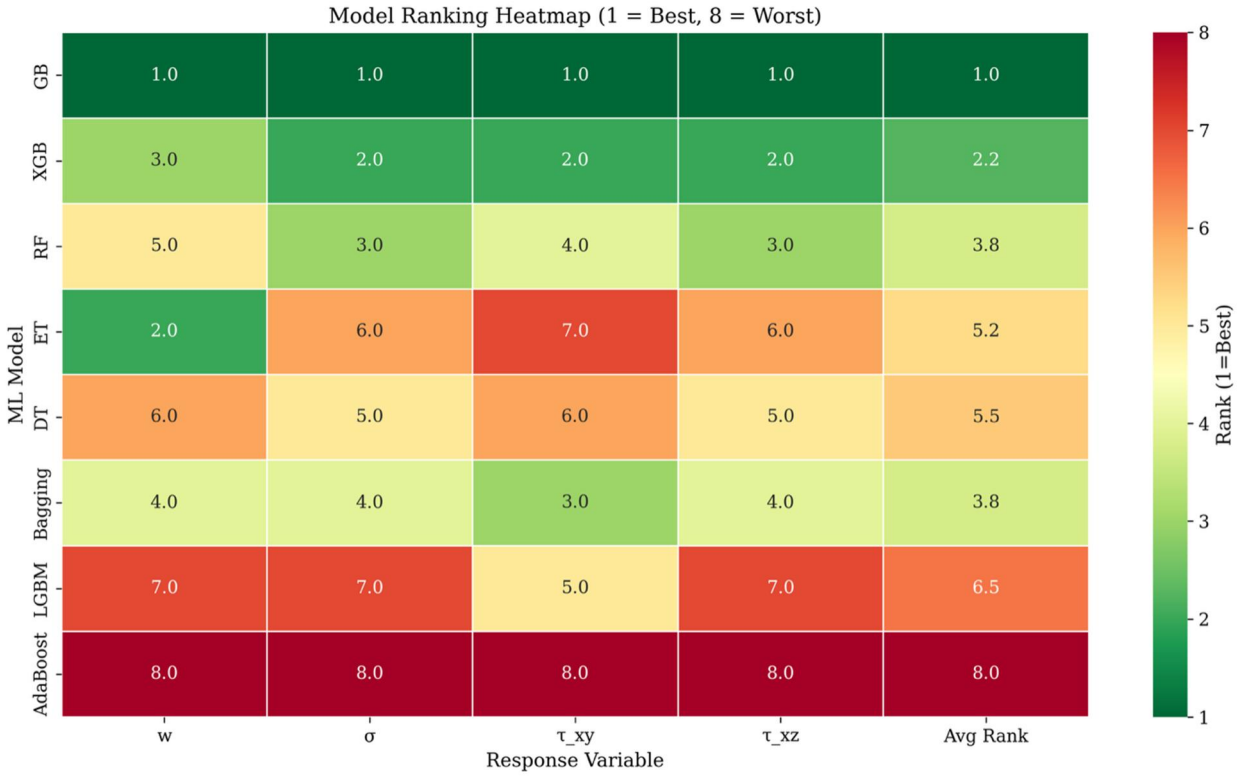

Figure 22. Heatmap of model performance rankings across all response variables and evaluation metrics (R^2, RMSE, MAE). Cells are color-coded from dark green (rank 1, best performance) to dark red (rank 15, worst performance). The Gradient Boosting Regressor achieves rank 1 or rank 2 consistently across all response-metric combinations, while linear models (Linear Regression, Ridge, Lasso, Elastic Net) occupy the lowest ranks. This aggregate view confirms that the performance advantage of Gradient Boosting is not specific to any single target or error metric.

shows the transverse shear stress ($\tau_{x\not z}$), confirming consistent zero-centered distributions with Gradient Boosting exhibiting the smallest dispersion and thinnest tails. Overall, Figure 20(a–d) demonstrates that while all three models perform reliably, Gradient Boosting achieves superior accuracy by minimizing both variance and extreme prediction errors.

Figure 21(a) presents the Taylor diagram for central deflection (w), where ensemble models cluster closest to the reference point, indicating high correlation and low standard deviation error. Figure 21(b) shows the corresponding diagram for normal stress (σ), with Gradient Boosting and XGBoost positioned nearest to the ideal location, reflecting superior predictive accuracy. Figure 21(c) illustrates the Taylor diagram for in-plane shear stress (τ_{xy}), where a larger spread among models is observed, indicating relatively higher variability in prediction performance. Figure 21(d) presents the transverse shear stress ($\tau_{x\not z}$), where most ensemble models again cluster tightly near the reference point, demonstrating strong agreement with actual values. Overall, Figure 21(a–d) confirms that ensemble-based models consistently achieve higher correlation, lower error, and better agreement with reference data compared to conventional models across all response variables. Figure 22 presents a comprehensive ranking heatmap of all 15 models scored by their aggregate performance across R^2, RMSE, and MAE for all four targets, confirming that Gradient Boosting occupies the top overall rank while linear models occupy the bottom four positions consistently. Figure 21(a–d) presents a Taylor diagram for central deflection, whereas Figure 22 compiles an aggregate ranking heatmap for all models and targets.

5.10. Hyperparameter sensitivity

The sensitivity of the Gradient Boosting R^2 on the estimators is shown. The performance of all four targets increases quickly with the number of trees between the range of 10 and approximately 100, then levels off, and the additional trees get relatively lower returns. The plateau is observed to happen with 200 estimators, which is the estimation taken in this research. This comparison proves the statement that the chosen hyperparameter configuration is close to the performance limit, and the results are not very sensitive to a minor variation in the size of the ensemble. The fact that the monotonic increase in ensemble size also shows that the lack of overfitting, which would be reflected in the fall in cross-validated R^2 at large sizes, does not occur. The sensitivity of Gradient Boosting cross-validated R^2 to the number of estimators is shown in Figure 23(a–d), demonstrating a rapid performance gain between 10 and 100 trees, followed by a plateau near the chosen configuration of 200 estimators, with no sign of overfitting at larger ensemble sizes. Figure 23(a) shows the sensitivity of cross-validated R^2 for central deflection (w) with respect to the number of estimators, where performance improves rapidly up to around 100–200 trees before reaching a plateau. Figure 23(b) presents the corresponding trend for normal stress (σ), with R^2 approaching unity and stabilizing beyond 200 estimators.

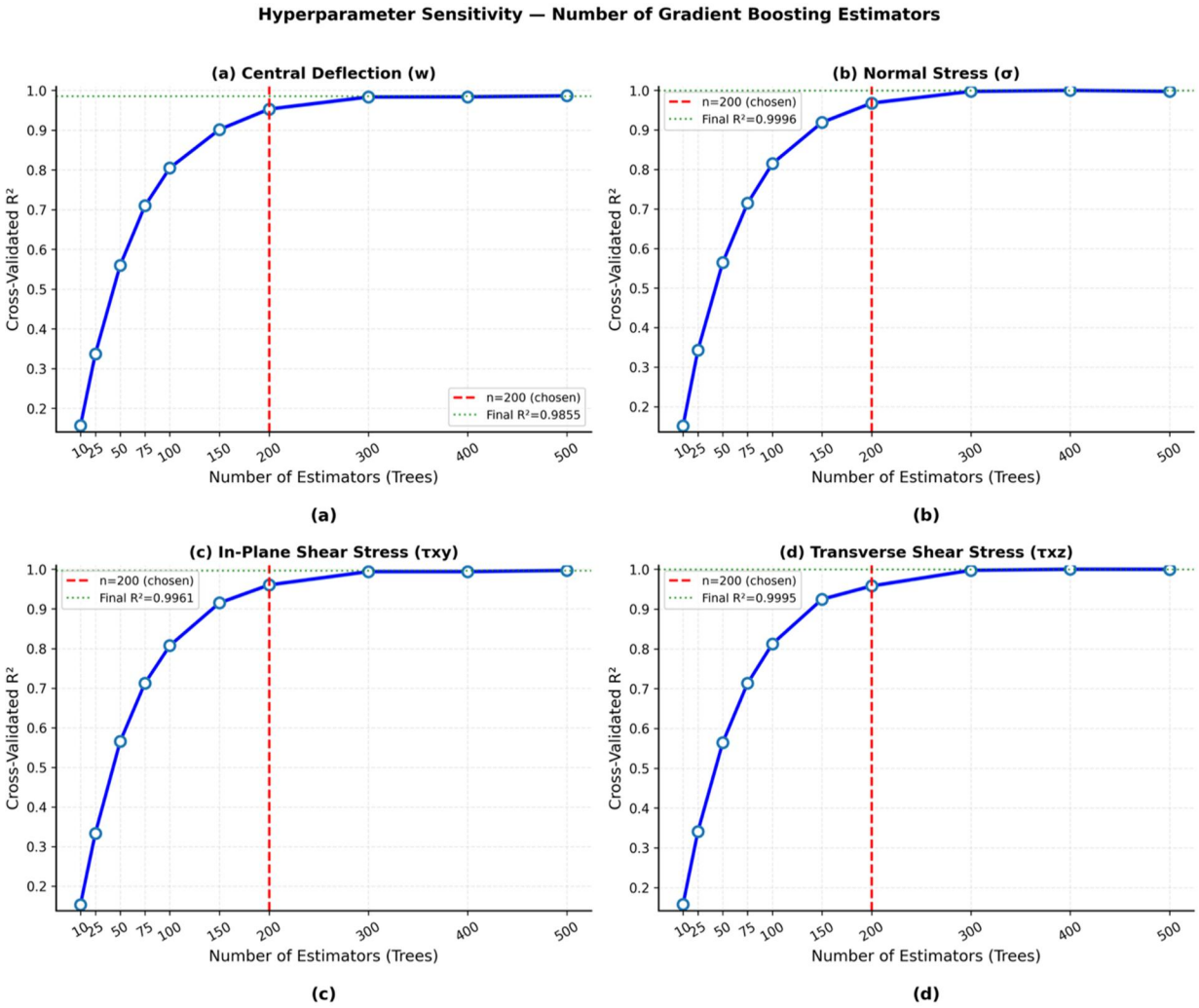

Figure 23. Sensitivity of the 10-fold cross-validated R^2 to the number of gradient boosting estimators (trees) for each of the four response variables: central deflection (w), normal stress (σ), in-plane shear stress (τ_{xy}), and transverse shear stress (τ_{xz}). Performance improves rapidly up to approximately 100 estimators and stabilizes near 200 estimators—the value used in this study—indicating diminishing returns beyond this point. The monotonically increasing cross-validated R^2 with ensemble size confirms that the chosen configuration avoids overfitting, as overfitting would manifest as a decline in validation R^2 at large ensemble sizes.

Figure 23(c) illustrates the behavior for in-plane shear stress (τ_{xy}), where a similar convergence pattern is observed, though with slightly slower initial improvement. Figure 23(d) shows the transverse shear stress (τ_{xz}), again confirming rapid performance gain followed by stabilization. Overall, Figure 23(a–d) demonstrates that model accuracy saturates beyond approximately 200 estimators, validating the selected hyperparameter choice and indicating no significant benefit from further model complexity.

6. Conclusions

This paper compared fifteen machine learning algorithms to predict the overall bending behavior of functionally graded carbon nanotube reinforced composite plates in four loading conditions. The data set was 144 different loading type-CNT volume fraction-width thickness ratio-CNTPattern-pattern combinations and four response variables, which included: central deflection, normal stress, in-plane shear stress and transverse shear stress. The results lead to the following conclusions:

- The Gradient Boosting Regressor had the best predictive accuracy among all four response variables, with the value of R^2 of 0.9855 (central deflection), 0.9996 (normal stress), 0.9961 (in-plane shear stress), and 0.9995 (transverse shear stress). XGBoost came second to last, then the Random Forest, and Extra Trees.
- Linear regression models (Ridge, Lasso, and Elastic Net) were found to perform poorly on all the targets, with an R^2 of 0.20 to 0.63. This proves that the correlation existing between the design parameters and the plate response is highly nonlinear and needs models that can portray the complex interactions.
- The width-to-thickness ratio was found to have the most impact on making predictions of deflection (over 85% importance), and the CNT distribution pattern showed the greatest effect on making predictions of stresses. The secondary, but not negligible, roles were played by loading type and volume fraction.
- Learning curve analysis established that the 144-sample dataset has enough information to allow the Gradient Boosting model to stabilize in its generalization with little

more information likely to be obtained in the current parameter space.
- The trained surrogate model saves the calculation time of one prediction from minutes (analytical solution) to less than one millisecond, which allows it to be deployed in real-time design screening and multi-objective optimization processes. The suggested data-driven model proves that the ensemble tree-based algorithms, in particular, gradient boosting, can be used as both precise and computationally safe estimates of structural examination of FG-CNTRC plates.

The proposed data-driven modeling framework offers several distinct advantages over conventional analytical and numerical approaches for analyzing FG-CNTRC plates. One of the most significant benefits is its computational efficiency, as the trained machine learning models provide near-instant predictions once developed, thereby eliminating the need for repeated finite element simulations for each new configuration. This is particularly advantageous in applications involving large-scale parametric studies, optimization, or real-time design evaluation. In addition, the framework demonstrates high predictive accuracy, with ensemble-based models such as Gradient Boosting achieving R^2 values as high as 0.9996 for stress prediction, which is comparable to high-fidelity numerical solutions. Another key advantage is the ability of machine learning models to capture complex nonlinear relationships among multiple input parameters—such as loading conditions, CNT distribution patterns, and geometric ratios—where traditional linear or simplified analytical models often fail. Furthermore, the inclusion of feature importance analysis enhances the interpretability of the results by identifying the dominant parameters governing structural behavior, thereby providing valuable physical insights. The framework is also flexible and scalable, allowing the integration of additional parameters or extension to other composite systems without significant reformulation.

However, the proposed approach also has certain limitations when compared to conventional methods. The primary disadvantage is its dependence on the quality and range of the training dataset, as the predictive capability of the model is inherently limited to the domain represented by the input data. Unlike physics-based analytical or finite element models, which are grounded in fundamental governing equations and can be extrapolated with caution, machine learning models may exhibit reduced reliability when applied to unseen configurations outside the training space. Additionally, the approach involves an initial computational cost associated with dataset generation, particularly when high-fidelity simulations are required to produce training data. Another limitation is the reduced physical transparency of some machine learning models, especially ensemble methods, which are often considered "black-box" in nature, although this is partially mitigated through feature importance analysis. Moreover, while the model demonstrates robustness with respect to hyperparameter variations, careful tuning and validation are still necessary to ensure optimal performance. This framework will be expanded to the dynamic response quantities (natural frequencies and mode shapes), thermal loading effects, and larger datasets produced with the three-dimensional finite element simulations in future work to further expand the coverage of the design space.

In comparison, traditional analytical methods offer clear physical insight and generality but are often limited by simplifying assumptions, whereas finite element methods provide high accuracy and general applicability at the expense of high computational cost. The present data-driven approach effectively bridges this gap by offering a balance between accuracy and efficiency, making it particularly suitable for rapid design exploration and engineering applications where repeated simulations are impractical.

Supplementary data

The Excel workbook (Supplementary_Data_FG_CNTRC_ML.xlsx) provides the complete numerical data underlying this study across nine dedicated sheets. Sheet S1 contains the full 144-configuration analytical dataset generated *via* HSDT-based Navier solution, tabulating all four mechanical response variables (central deflection, normal stress, in-plane shear stress, and transverse shear stress) for every combination of loading type, CNT volume fraction, b/h ratio, and CNT distribution pattern. Sheets S2A–S2D report the 10-fold cross-validated R^2, RMSE, MAE, and MAPE of all 15 regression algorithms for each response variable individually, with models ranked in descending order of R^2; Sheet S3 consolidates all 60 model–target performance records into a single cross-reference table. Sheet S4 provides the Friedman non-parametric test statistics (χ^2 and p-values), confirming that the observed performance rankings are statistically significant ($p < 0.001$ in all cases). Sheet S5 reports the mean absolute SHAP feature importance values for each input feature across all four response variables as derived from the trained Gradient Boosting surrogate model.

Acknowledgement

The authors would like to express their sincere gratitude to the Data Analytics and Research Lab at NICMAR University for providing the necessary resources and research environment that significantly contributed to the successful completion of this study. The authors also acknowledge Noida International University, Graphic Era (Deemed to be University), and G.L. Bajaj Institute of Technology and Management for extending the research facilities and academic support required for carrying out this work.

Author contributions

CRediT: **Surya Dev Singh**: Conceptualization, Supervision, Validation, Writing – original draft; **Pradyut Anand**: Conceptualization, Data curation, Formal analysis, Visualization, Writing – original draft; **Suresh Pratap**: Investigation, Methodology, Resources, Software, Validation, Writing – original draft; **Kul Sharma**: Visualization, Writing – review & editing; **Md Mahmudul Hasan**: Validation, Visualization, Writing – review & editing.

Disclosure statement

The authors declare that they have no known competing financial interests or personal relationships that could have appeared to influence the work reported in this paper.

Funding

There is no funding received for carrying out this project work.

Data availability statement

The consolidated dataset required to reproduce the findings of this study is available as supplementary material accompanying this article.

References

[1] K.M. Liew, Z.X. Lei, and L.W. Zhang, Mechanical analysis of functionally graded carbon nanotube reinforced composites: a review, Compos. Struct., vol. 120, pp. 90–97, 2015. DOI: 10.1016/j.compstruct.2014.09.041.

[2] H.-S. Shen, Nonlinear bending of functionally graded carbon nanotube-reinforced composite plates in thermal environments, Compos. Struct., vol. 91, no. 1, pp. 9–19, 2009. DOI: 10.1016/j.compstruct.2009.04.026.

[3] P. Phung-Van, M. Abdel-Wahab, K.M. Liew, S.P.A. Bordas, and H. Nguyen-Xuan, Isogeometric analysis of functionally graded carbon nanotube-reinforced composite plates using higher-order shear deformation theory, Compos. Struct., vol. 123, pp. 137–149, 2015. DOI: 10.1016/j.compstruct.2014.12.021.

[4] P. Zhu, Z.X. Lei, and K.M. Liew, Static and free vibration analyses of carbon nanotube-reinforced composite plates using finite element method with first order shear deformation plate theory, Compos. Struct., vol. 94, no. 4, pp. 1450–1460, 2012. DOI: 10.1016/j.compstruct.2011.11.010.

[5] Z.X. Lei, J.L. Yu, and K.M. Liew, Free vibration analysis of functionally graded carbon nanotube-reinforced composite cylindrical panels, IJMSE, vol. 1, pp. 36–40, 2013. DOI: 10.12720/ijmse.1.1.36-40.

[6] L.W. Zhang, Z.X. Lei, K.M. Liew, and J.L. Yu, Static and dynamic of carbon nanotube reinforced functionally graded cylindrical panels, Compos. Struct., vol. 111, pp. 205–212, 2014. DOI: 10.1016/j.compstruct.2013.12.035.

[7] G. Tam, and B. Yön, Assessment of seismic fragility of reinforced concrete buildings retrofitted with steel bracing elements: a numerical study, Struct. Eng. Mech., vol. 96, no. 2, pp. 117–129, 2025. DOI: 10.12989/sem.2025.96.2.131.

[8] K. Bousmaha, S.A. Belalia, S.M. Chorfi, A. Tounsi, M.A. Al-Osta, and A.E. Alluqmani, On the dynamic behavior of plates made of porous advanced materials reinforced with carbon nanotubes using a p-version of finite element method, Mech. Based Des. Struct. Mach., vol. 54, no. 1, pp. 2534679, 2026. DOI: 10.1080/15397734.2025.2534679.

[9] A. Beitollahi, M. Janghorban, Y. Bazargan-Lari, and A. Tounsi, On the variable length scale parameter for agglomeration of nanoparticles in nanocomposites, Proc. Inst. Mech. Eng. Part C: J. Mech. Eng. Sci., vol. 239, no. 10, pp. 3828–3850, 2025. DOI: 10.1177/09544062241308513.

[10] H. Youzera, S.A. Meftah, A. Tounsi, M.A. Salem, K.M. Khedher, and M. Yaylacı, Free vibration analysis of sandwich cylindrical shells with functionally graded carbon nanotube-reinforced composite face sheets using the differential quadrature (DQ) method, Acta Mech., vol. 236, pp. 1395–1410, 2025. DOI: 10.1007/s00707-025-04230-y.

[11] A. Zerrouki, M. Zidour, A. Tounsi, A. Tounsi, Z. Belabed, A.A. Bousahla, M.A. Salem, and K.M. Khedher, Buckling behavior of nonlinear FG-CNT reinforced nanocomposite beam resting on Winkler/Pasternak foundation, Comput. Concrete., vol. 34, no. 3, pp. 297–305, 2024.

[12] D.W. Abueidda, S. Koric, N.A. Sobh, and H. Sehitoglu, Deep learning for plasticity and thermo-viscoplasticity, Int. J. Plast., vol. 136, pp. 102852, 2021. DOI: 10.1016/j.ijplas.2020.102852.

[13] C.-T. Chen, and G.X. Gu, Machine learning for composite materials, MRS Commun., vol. 9, no. 2, pp. 556–566, 2019. DOI: 10.1557/mrc.2019.32.

[14] X. Liu, S. Tian, F. Tao, and W. Yu, A review of artificial neural networks in the constitutive modeling of composite materials, Compos. Part B: Eng., vol. 224, pp. 109152, 2021. DOI: 10.1016/j.compositesb.2021.109152.

[15] B. Daou, A. Lebée, F. Kaddah, and K. Sab, Prediction of thick plate properties of CLT and innovative panels through machine learning algorithms, Eng. Struct., vol. 322, pp. 119048, 2025. DOI: 10.1016/j.engstruct.2024.119048.

[16] B.B. Mishra, A. Kumar, P. Samui, and T. Roshni, Buckling of laminated composite skew plate using FEM and machine learning methods, EC, vol. 38, no. 1, pp. 501–528, 2021. DOI: 10.1108/EC-08-2019-0346.

[17] Vaishali, P. K. Karsh, S. Kushari, R. R. Kumar, and S. Dey, Stochastic free vibration and impact responses of functionally graded plates: a support vector machine learning model approach. J. Vib. Eng. Technol., vol. 11, no. 7, pp. 2927–2943, 2023. DOI: 10.1007/s42417-022-00721-7.

[18] M. Raissi, P. Perdikaris, and G.E. Karniadakis, Physics-informed neural networks: a deep learning framework for solving forward and inverse problems involving nonlinear partial differential equations, Comput. Phys., vol. 378, pp. 686–707, 2019. DOI: 10.1016/j.jcp.2018.10.045.

[19] W. Wang, and H.-T. Thai, A physics-informed neural network framework for laminated composite plates under bending, Thin. Walled Struct., vol. 210, pp. 113014, 2025. DOI: 10.1016/j.tws.2025.113014.

[20] C. Liu, Q. He, A. Zhao, T. Wu, Z. Song, B. Liu, and C. Feng, Operator learning for predicting mechanical response of hierarchical composites with applications of inverse design, Int. J. Appl. Mech., vol. 15, no. 04, pp. 2350028, 2023. DOI: 10.1142/S175882512350028X.